catalysts

MDPI

Review

Oxygen-Deficient Engineering for Perovskite Oxides in the Application of AOPs: Regulation, Detection, and Reduction Mechanism

Jiayu Yu [1], Huanhuan Li [1], Naipeng Lin [1], Yishu Gong [1], Hu Jiang [2], Jiajia Chen [1], Yin Wang [1,*] and Xiaodong Zhang [1,*]

[1] School of Environment and Architecture, University of Shanghai for Science and Technology, Shanghai 200093, China
[2] School of Materials Science and Engineering, Shanghai University, Shanghai 200444, China
* Correspondence: 625xiaogui@163.com (Y.W.); fatzhxd@126.com (X.Z.)

Abstract: A perovskite catalyst combined with various advanced oxidation processes (AOPs) to treat organic wastewater attracted extensive attention. The physical and chemical catalytic properties of perovskite were largely related to oxygen vacancies (OVs). In this paper, the recent advances in the regulation of OVs in perovskite for enhancing the functionality of the catalyst was reviewed, such as substitution, doping, heat treatment, wet-chemical redox reaction, exsolution, and etching. The techniques of detecting the OVs were also reviewed. An insight was provided into the OVs of perovskite and reduction mechanism in AOPs in this review, which is helpful for the reader to better understand the methods of regulating and detecting OVs in various AOPs.

Keywords: oxygen vacancy; advanced oxidation processes; perovskite; detect technologies; regulate methods

Citation: Yu, J.; Li, H.; Lin, N.; Gong, Y.; Jiang, H.; Chen, J.; Wang, Y.; Zhang, X. Oxygen-Deficient Engineering for Perovskite Oxides in the Application of AOPs: Regulation, Detection, and Reduction Mechanism. *Catalysts* **2023**, *13*, 148. https://doi.org/10.3390/catal13010148

Academic Editor: Hamidreza Arandiyan

Received: 21 December 2022
Revised: 4 January 2023
Accepted: 5 January 2023
Published: 9 January 2023

1. Introduction

Meeting the imperious demand for purification of sewage was crucial step to ensure an eco-friendly development. Great efforts were contributed to looking for the cost-effective catalysts to purify wastewater. At present, there were many water treatment methods, such as biological treatment, physical treatment, sludge treatment, and chemical treatment, etc. Among these techniques, advanced oxidation processes (AOPs) [1,2] were extensively studied for the oxidation of the kinds of deleterious matters in wastewater [3]. AOPs were widely used because of their rapid reaction, high redox potential, etc. They could achieve efficient degradation of organic matter by producing highly reactive oxygen species (ROS) [4], such as hydroxyl radicals (•OH) [5], sulfate radicals ($SO_4\bullet^-$) [6], and others. AOPs included Fenton processes, photocatalysis, electrochemical advanced oxidation processes, ozonation, persulfate-based oxidation, and so on [7,8].

Anion defects in perovskite played a very important role in catalysis. Reactive oxygen species produced by AOPs were closely related to OVs, which were one of the anion defects. The oxygen atoms were missed by oxygen-deficient perovskite, which was named oxygen vacancies (OVs). OVs as specific reaction sites could change the structure of a material, altering surface electronic and chemical structures [9], translating to attach oxygen gas to superoxide radicals. OVs played an important role in photocatalysis, energy storages, electrocatalysis, etc. At present, the research of OVs was mainly focused on metal oxide catalysts.

Perovskite was a kind of metal catalysts in AOPs reaction, while improving OVs of perovskites was an effective way to improve their functions. Perovskites have a low price, high stability, and excellent catalytic activity, which could serve as desirable catalysts to initiate AOPs for purification of organic wastewater. Structurally, ABO_3 was the molecular

formula of perovskites. The position of A was occupied by rare earth or alkali metals, and the B position was occupied by active transition metals [10]. The position of A or B could be replaced by the kinds of metals, which could change their physical and chemical properties [11].

Therefore, to improve the reaction efficiency of AOPs and make the OVs in perovskite catalyst play a greater role, it was necessary to deeply understand the regulation, detection, and reaction mechanism of OVs. Then, the innovation of this paper lied in the following: first of all, the basic knowledge of OVs in perovskite, which are involved in the structure of perovskite, and characteristic was given. In the next place, the strategies to detect OVs were highlighted. Finally, the focus was on improving OVs of perovskites for the performance of a catalyst in AOPs. This review would help to better understand the mechanism of OVs in perovskite promoting degradation of organic pollutants in AOPs.

2. Perovskite Materials

Perovskite referred to a group of materials with a crystal structure similar to calcium titanate [12]. Perovskite oxides were widely used in electrocatalysis, photocatalysis, and membrane catalysis, etc. Types of perovskites and the catalyst rate in AOPs are shown in Table 1. The following was the introduction of perovskite and the role of OVs.

Table 1. Types of perovskites and the catalyst rate in AOPs.

Perovskite	Catalyst Dosage	AOPs	Organic Pollutants	Catalyst Rate	Ref.
Bi_2WO_6	50 mL of 20 mg/L CIP aqueous solution.	Photocatalyst	ciprofloxacin	90% at 6 h	[13]
$LaCu_{0.5}Co_{0.5}O_3$-$MMT_{0.2}/CN_x$	9.5 g/L	Microwave irradiation	Bisphenol A	98.7% at 6 min	[14]
$LaCoO_3$	10 mg of 50 mg/L 2,4-dichlorophenol	Sulfate Radical-Based AOPs	2,4-Dichlorophenol	99.8% at 25 min	[15]
$BiFeO_3$	0.5 g/L	Fenton-like	Rhodamine B	95.2% at 90 min	[12]
$LaMn_4O_x$	0.2 g/L	Ozonation	Oxalic acid	100% at 45 min	[12]
$La_2CuO_{4-\delta}$	0.7 g/L	Sulfate Radical-Based AOPs	Bisphenol A	96.7% at 60 min	[16]
$LaFe_{0.5}M_{0.5}O_3$-CA (M = Mn, Cu)	0.4 g/L	Microwave irradiation	Fuchsin basic	100% at 4 min	[17]
$LaNiO_3$	1 g/L	Wet air oxidation	Reactive Black	65.4% at 120 min	[18]

2.1. Structure of Perovskite

From the perspective of morphology, perovskite materials could be divided into three dimensions [19], such as metal–organic frameworks (Mofs) [20]. The ideal cubic symmetry of ABO_3 perovskite oxide is shown in Figure 1a. The BO_6 octahedral structure was formed by interlinking the angular oxygens, and the A-site cation occupied 12 sites around the BO_6 octahedron. Changing atoms at the A and B sites could improve the performance of perovskites [21]. There were about 73 alternative elements in the periodic table A and B occupy space, so the potential variety of perovskite materials was multiple [22].

The ionic radius of A was larger than that of B, and the reason for the variety of perovskite-type oxides was the existence of two cation sites of different sizes. To form a perovskite-type structure, the radii of ions at the position of A and B need to satisfy following Equation (1) [23]:

$$t = (r_A + r_O)/\sqrt{2}(r_B + r_O) \quad (1)$$

where t was a tolerance factor. r_A, r_B and r_O referred to the ionic radii of the position of A, B, and the oxygen anion, respectively.

2.2. The Role of Oxygen Vacancy in Perovskite

The primary structure of perovskite (ABO_3) could lead to the constituent elements to deviate from the 1:1:3 stoichiometric ratio and constitute a new non-stoichiometric structure. When A or B sites were partially replaced, changes in surface vacancies and valence might be formed and induce the oxygen-deficient in perovskite, $ABO_{3\pm\delta}$ ($0 < \delta \leq 1$) [24]. The oxygen atoms were missed by oxygen-deficient $ABO_{3-\delta}$ perovskite, which was named oxygen vacancies (OVs) [25]. The neutral and charged oxygen vacancies are expected to be stable under tensile strain and compressive strain, respectively [26].

The OVs probe in perovskite catalysts increased significantly (Figure 1b), and a number of recent articles of OVs was listed. OVs' detect technology [27], calculation method [26,28,29], and regulate method [30–32] were shown. OVs played pivotal roles in the catalysis field of perovskite. In most cases, the catalytic effect of the perovskite in AOPs had a direct relationship with the amount of OVs [33]. In general, the excellent catalytic performance of perovskite could be found in the following aspects. Firstly, maintaining the stable structure of perovskite and introducing OVs could be achieved by doping other metal ions at the position of A or B. Secondly, an adsorbed oxygen migration ability was closely related to catalytic performance [34]. Enhanced redox capacity could promote the migration of surface reactive oxygen ions through the formation of OVs [35]. The roles that OVs played in different AOPs responses follow.

It was evident that OVs as the active sites could lead to some new energy levels [36]. For the purpose of escalating activity of the catalyst, OVs became a key player in the development of oxide-based technologies used in electronics and spintronics [37,38]. An appropriate shoot in OVs was conducive to get rid of organic pollutants. The regulation of OVs was generally applied in the field of battery or catalysis; oxygen vacancy improved the catalytic activity of catalysts in different ways [39]. The application of different AOPs was as follows:

(1) Photocatalysis. Since defects were ubiquitous in catalytic materials and could modulate the electronic structure and optical properties of most catalysts, photocatalytic performance could be improved by various types of defect engineering [40]. Wu et al. [41] discovered OVs formed at the atoms of BiOBr would create a new layer of defects and then expanded the optical absorption range in the visible light. The OVs were advantageous for the photogenerated carrier separation efficiency and thus soared the photocatalytic properties of BiOBr. In addition, the OVs could provide an adsorption site in catalysts, and the pollutants were rapidly adsorbed [14,42].

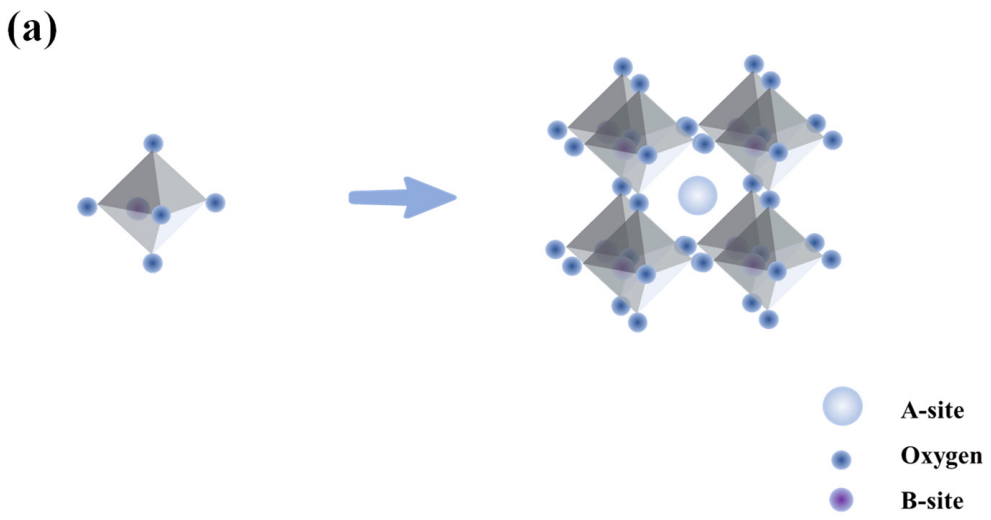

Figure 1. *Cont.*

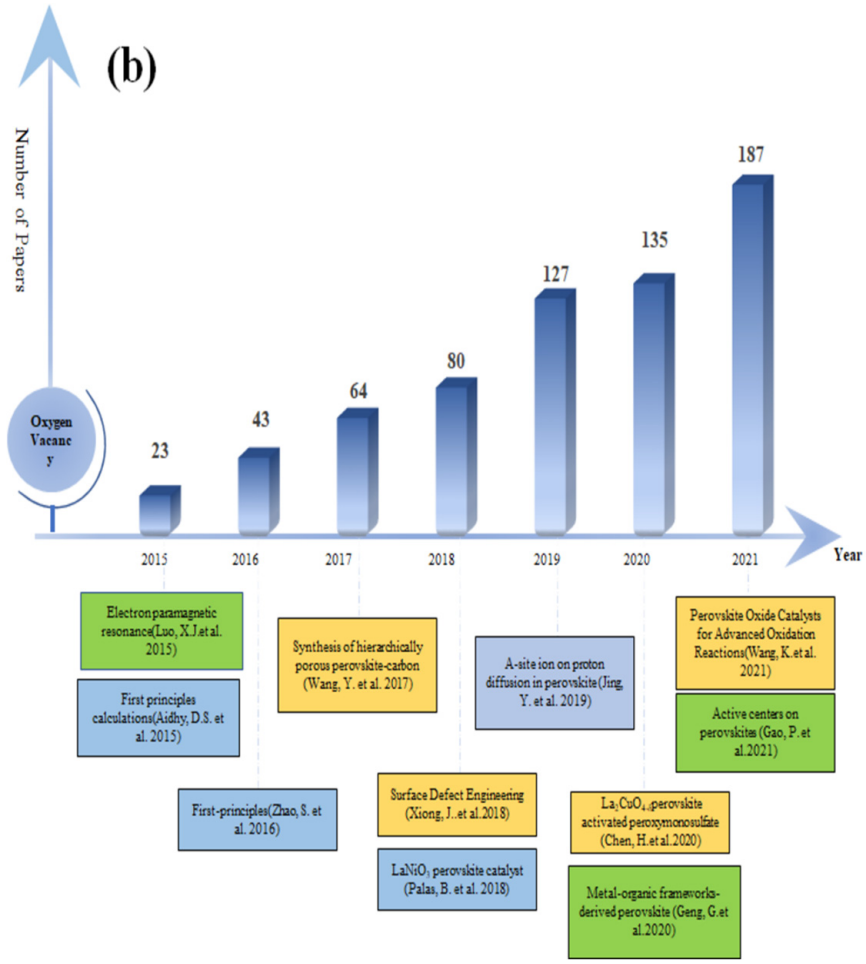

Figure 1. (**a**) Crystal structure of a cubic perovskite with a chemical formula of ABO_3 and (**b**) the number of papers abstracted by the database Web of Science for topic keywords "perovskite catalyst and oxygen vacancy" and some representative work on perovskite application in advanced oxidation in recent years [10–12,14–18,23,26–28].

(2) Electrocatalysis. A new method was proposed to escalate the activity of N_2 reduction reaction by adjusting the OVs caused by the A-site cations. Chu et al. [43] proposed that the related advantages of OVs rose the activity of N_2 reduction reaction, such as the activation of reactive species promoted by OVs, thus optimizing the reaction pathway. The yield of NH_3 was 22.1 $\mu g \cdot h^{-1} \cdot mg^{-1}{}_{cat}$ with the increase in OVs. The Faraday efficiency at −0.3 V was 25.6%. They were 2.2 times and 1.6 times of the perovskite rate without improving OVs.

$LaFeO_3$ perovskite was tuned OVs as an efficient electrocatalyst. The oxygen evolution reaction (OER) performance was extremely intensified. The highest OER activity was affected by a moderate concentration of OVs in $LaFeO_3$.

(3) Microwave catalysis. A new type of double perovskite was prepared in situ by successively adding montmorillonite and g-C_3N_4 intercalation by Wang et al. [44]. A large number of hot spots were generated by $LaCu_{0.5}Co_{0.5}O_3$ (LCCO) on its surface and bisphenol A (BPA) was degraded after absorbing a large amount of microwave energy (Figure 2). It showed excellent microwave catalytic ability on account of a more diminutive pore, a bigger specific area, and the highest chemisorption surface oxygen concentration [45]. Microwave could excite the surface-active sites of the catalyst to generate oxidized free radicals, thus degrading bisphenol A via electron-hole transport.

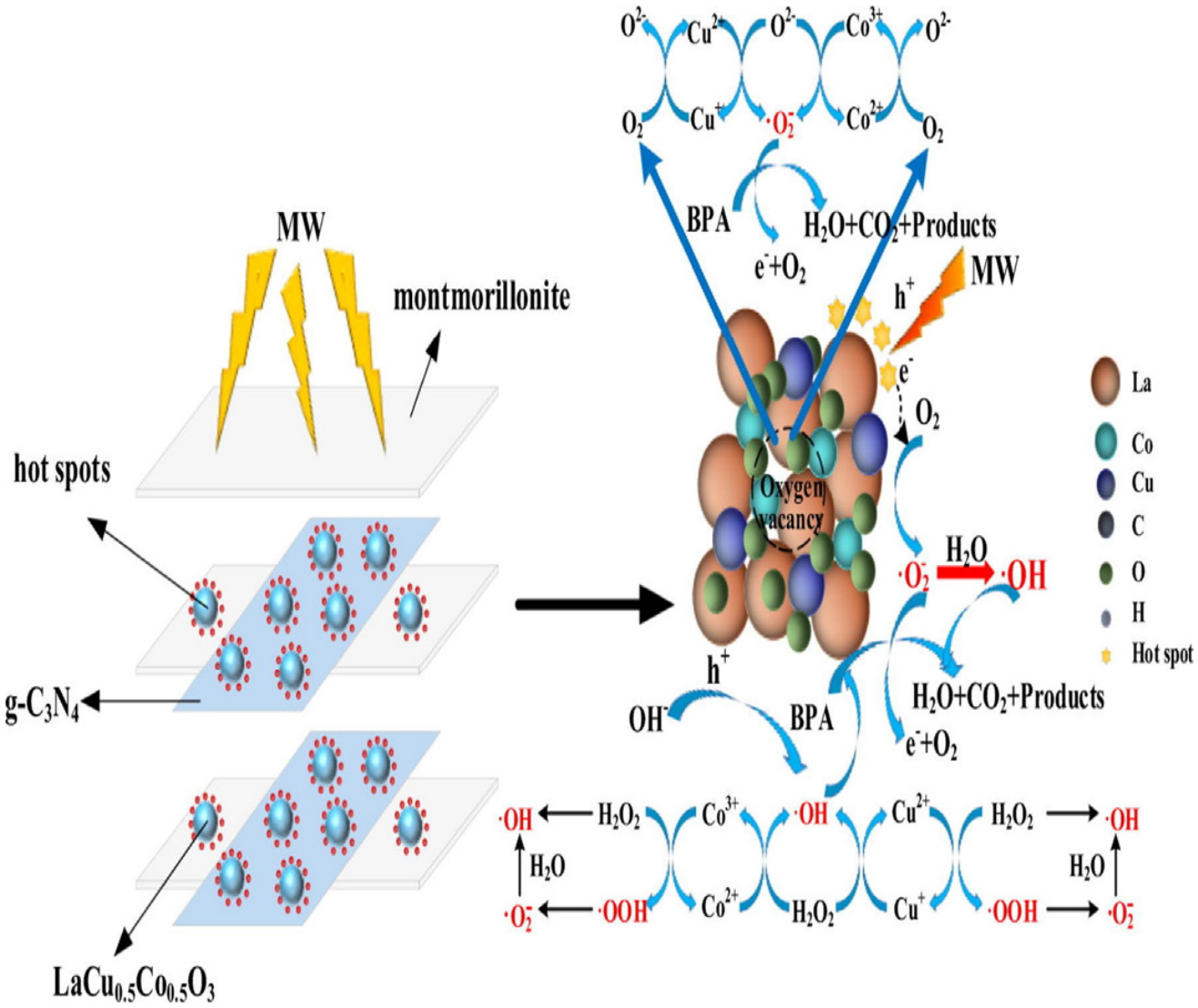

Figure 2. Possible BPA degradation mechanism over $LCCOM_{0.2}/CN_{0.075}$ under MW irradiation [44].

3. Approaches to Regulate Oxygen Vacancy in Perovskite

Now, there were many methods to regulate oxygen defects, as shown in Table 2, in which OVs in perovskites could be induced during crystal growth or through post-treatment. Many effective defect preparation methods were developed to improve OVs: ion substitutions, heat treatment, exsolution, etching, ion doping, wet-chemical redox reactions, etc. Theoretically, chemical defects could alter the structure of perovskite, decrease the activation energy of the catalyst, and improve the diffusion dynamics of its ions.

Table 2. Summary of approaches to improving oxygen vacancies in perovskite.

Classification	Perovskite	Preparation Method	Organic Pollutants	Synthesis Parameters	Catalyst Rate	Ref.
Cation substitutions: A-cation	$La_{1-x}AgxCoO_3$	EDTA−citric acid complexation	Soot	$LaCoO_3$ was partially replaced with Ag^+. PH = 7, Calcination: 700 °C, 5 h	99%	[45]
	$La_{2-x}K_xNiCoO_6$	Colloidal crystal template	Soot	The partial substitution of A-site (La) with low-valence potassium (K) ions. Calcination: 346 °C	99.3%	[46]
	La_2NiFeO_6	Modified sol–gel method (Pechini method)	Toluene	Heating:180 °C, 10 h Drying: 70 °C, 1 h Calcination: 650 °C, 5 h;	90%	[47]
Cation substitutions: B-cation	$LaCoO_{3-\delta}$	Sol–gel method	Bisphenol A	Drying: 60 °C, overnight annealed in air: 700 °C, 2 h Calcination: 800 °C	90%	[48]
Ion non-stoichiometry	$Ca_{1.1}ZrO_3$	coprecipitation calcination method	M-cresol	Heating:100 °C, Drying: 120 °C, 12 h Calcination: 900/1100 °C, 6 h;	100%	[49]
	$La_{1.15}MnO_{3+d}$	Sol–gel method	Rhodamine B	pre-decomposed at 180 °C, for 6 h Calcination: 800 °C, 5 h;	100%	[50]
Chemical reduction	$NaNbO_3$	Solid–state reaction	Methyl blue (MB)	Calcination: 325–500 °C, 61 h, N_2 atmosphere Heating rate:5 °C min^{-1} Drying: 60 °C, vacuum atmosphere	Enhanced by almost 2.4 times	[50]
Exsolution	$Pr_{0.5}Ba_{0.5}Mn_{0.85}Co_{0.15}$	B-metal ex-solution	CO	Heating: 300 °C, Calcination: 600 °C, 4 h	82.5%	[51]
Etching	$La_{0.8}Sr_{0.2}CoO_3$	Etching by Oxalic acid	CH_4	Calcination: 700 °C, 2 h; Drying: 55 °C	-	[52]

3.1. Ion Substitutions

The substitution of A and/or B site ions by other elements was a traditional method of improving OVs in materials, which could release lattice oxygen. $AA_xBB_xO_{3-d}$ was represented by the defective perovskite, where A_x and B_x, respectively, referred to the dopant elements that replaced A and B. Ordinarily, OVs were fabricated by A-site cation substitution, while B-site cation substitution mainly changed the structure of the A site by bringing into play the electronic structure to generate OVs. The lattice defects could be generated by regulating the ratio; the specific optimization was used to adjust the properties of the catalyst and further change its physical and chemical characteristics [49]. Li et al. [53] added fifteen percent of A-site cations into the oxide lattice of $LaMnO_3$, which allowed the successful introduction of OVs and the modification of catalytic properties in perovskite. That ballooned the catalytic activity of PMS for the degradation of rhodamine B. The LMO-PMS system was capable of catalyzing the reaction under the condition of most pH ranges. A perovskite catalyst could be flexibly doped with B-site cations, mainly transition metal elements. B-site transition metal elements, such as Co and Ni, were usually active centers interacting with reaction intermediates, promoting the catalytic reaction and being small size.

He et al. [47] used an EDTA-citric acid complexation method to made a series of $La_{(1-x)}Ag_xCoO_3$ (LACO). LACO had the largest solubility range and the best catalytic activity when x = 0.25. The improvement of soot's cyclic oxidation properties indicated that the OVs were more easily formed, and the lattice oxygen transport was enhanced after Ag^+ replacing the A-site ions at low temperature.

Liang et al. [54] prepared $LaCoO_{3-\delta}$ (LCO) perovskite catalyst by using the sol–gel method, which boosted the improvement of catalytic properties. The B-site cation defect was in favor of the activation of PMS, resulting in a higher first-order kinetic rate of LCO because sulfate played a vital role in the decomposition of bisphenol A, and OVs formed on LCO raised the reactivity.

$Sr_{0.95}Nb_{0.1}Co_{0.9-x}Ni_xO_{3-\delta}$ catalysts with trifunctional electrocatalytic activity were synthesized by Islam [55], who suggested that different ratios of A:B showed distinct results. The catalytic activity decreased in the situation of A:B = 1, but when A:B < 1, it was possible to achieve a better condition for formatting OVs.

3.2. Ion Doping

In addition to a single type of ion substitutions, the catalyst could be doped with anion or cation to improve the activity. The kinds of A-site perovskite-type catalysts (Ce-doped La and Fe) using a sol–gel method were further studied by Ren et al. [56]. They found that catalytic properties of Ce-doped $La_{1-x}Ce_xFeO_3$ for TOC removal in ozonation was significantly improved, and the optimal catalytic performance was when x = 0.2. Higher oxygen content in the lattice led to a higher catalytic activity. The reason for the high efficiency of ozone oxidation, researchers speculated, might be the decomposition of O_3 into free radicals (ROS) on the surface of a catalyst. Adding the catalyst was more beneficial to the decomposition of ozone translating into ROS and had better ozone degradation capability.

Double perovskite $La_{2-x}K_xNiCoO_6$ was prepared by a colloidal crystal template method, which was a catalyst for 3D ordered microporous structure by Zhang et al. [48]. Bimetallic nanoparticles with high surface area and active site density can improve reduction efficiency [57]. The doping of K ions became a key step to promote the oxidation of NO to NO_2 because this step shot the surface oxygen density of the catalyst during the purification of catalytic soot. With the same as a double perovskite-type catalyst, La_2NiFeO_6 was synthesized by a one-step hydrothermal method, and it had nanorods morphology. The author's plan to adjust the surface oxygen activity was to dope nickel atoms because more OVs would be generated, which was conducive to the enhancement of catalytic performance of toluene catalytic oxidation [58].

Ding et al. [59] studied the formation of OVs in an A-site-doped $LaMnO_3$ catalyst (A = Sr, Ag, and Sn), observing and calculating the surface oxygen mobility. The presence of dopants promoted the formation of OVs and significantly decreased the activation energy of O_2 dissociation, which was due to the electron transfer between oxygen and the catalyst surface.

Theoretically, chemical defects could alter the structure of perovskite, decrease the activation energy of the catalyst, and improve the diffusion dynamics of its ions. Zhao et al. [60] prepared the $Pd/La_xSr_{0.3}MnO_3$ catalyst, and the influence of ratio on the structure of the catalyst was investigated. The results indicated that the A-Site defect perovskite could be regenerated more efficiently than the $SrCO_3$ phase under 300 °C. For the purpose of improving the ability of $CaZrO_3$ to catalyze ozone and adjust the stoichiometric deviation of A-site cations, Han et al. [61] showed that this method also changed the crystallinity of $CaZrO_3$.

Except for the cation doping, the addition of N, P, S, F, and other anions were also investigated with the aim of enhancing the activity of metal oxides. With S atom replacing the crystal O atoms in the lattice, the internal conductivity of the samples was improved, and a part of OVs were also formed. You et al. [62] synthesized the S-doped $SrIrO_3$ electrocatalyst, and the incorporation of S would reduce the activation energy and contribute to OER activity.

Han et al. [63] proposed to prepare F-doped Sr_2TiO_4($Sr_2TiO_{3.97}F_{0.03}$) to improve the photocatalytic activity in HER of the catalyst. Cropping the F-doping amount in the O position of $Sr_2TiO_{3.97}F_{0.03}$ resulted in good photocatalytic activity because of the increased OVs' concentration on the surface and reduced the charge carrier recombination, etc.

3.3. Heat Treatment

The heat treatment method was also a typical method to introduce defects. Heat treatment was mainly used to reduce atmosphere, reduce reagents (such as $NaBH_4$, N_2H_4, NaH, AI powder, etc.), reduce solvents (such as methanol, ethanol, ethylene glycol, etc.) and reduce flame in the preparation process.

In general, the escape of atoms could be accelerated by thermal treatment, thus introducing defects into the catalytic material. Annealing of metal oxides at high temperatures could be used to reduce atmosphere to produce more OVs, leading to a larger specific surface area and a higher charge density of perovskite.

Saloaro et al. [64] made double perovskite Sr_2FeMoO_6 by using an in situ annealing method to find out the changes in relatively small OVs. They suggested that other complex magnetic perovskites could also adopt the annealed with the intention of designing nanoscale defects.

Chen et al. [65] reported the layered perovskite-$Sr_{n+1}Ti_nO_{3n+1}$ (STO). In the case of STO acting as an oxygen diffusion barrier layer, they could reversibly adjust the concentration of OVs near the interface by high-temperature annealing or infrared laser heating. Yang et al. [66] synthesized $NaNbO_3$ with OVs in a well-controlled method. The catalyst became higher visible-light activities when OVs were introduced into the perovskite. Because a specific surface area became larger, charge density was higher for $NaNbO_3$. It was possible to use NH_3 gas or other reducing atmospheres to incorporate OVs into the perovskites at high temperatures. After thermal treatment of tetra butyl titanate precursor solution, calcining it in Ar and NH_3 for minutes, respectively, led to more OVs into the TiO_xN_y [67].

Sun et al. [68] used electron paramagnetic resonance (EPR) to detect OVs in Li_2MnO_3 (LMO), and the results clearly indicated that OVs were indeed present in the reduced samples. OVs in LMO were successfully introduced by the low-temperature reduction method.

3.4. Wet-Chemical Redox Reactions

Wet-chemical redox reactions were a liquid phase to participate in the reaction through chemical reactions to prepare materials, including precipitation method, sol–gel method,

and so on. Some reducants (such as $NaBH_4$) were used to produce the quantity of OVs [69]. A large number of vacancies could be produced in samples by introducing reductive reagents in the process of chemical synthesis or by heat treatment in the later stage and reducing fireworks treatment. The operation was simple and had an obvious effect on improving the properties of materials.

Sun et al. [70] introduced $La_{1-x}Ce_xFeO_{3-\delta}$ by coprecipitation into the CWAO process for the first time, which would cause changes in the species of reactive oxygen species and OVs in the perovskite. The results showed that when the molar ratio of Ce:(La and Ce) was greater than 0.4, the provskite had a high catalytic activity for the efficient degradation of acrylic acid by CWAO.

Zhang et al. [71] prepared $LaCoO_3/CeO_2$ by a sol–impregnation two-step method to purify the membrane concentrate of the coal chemical wastewater. With the addition of CeO_2, OVs formed in the charge balance process and the ratio of lattice oxygen (O_L)/surface activated oxygen (O_S) increased from 0.80 to 1.48, indicating that the defect of O_L on $LaCoO_3/CeO_2$ increased. Under the best operating conditions, the BOD_5:COD of the oxidized effluent was greatly increased, and the biodegradability of the oxidized effluent was greatly improved.

3.5. Exsolution

In the field of catalysts, compared with noble metals and simple oxides, perovskite had two inherent defects, which were a small specific surface area and an inert surface segregation. These disadvantages reduced the number and activity of surface-active sites, which might cut down the catalytic performance of perovskite to a certain extent [72]. In view of the above problems, exsolution was gradually adopted to create OVs. The method called exsolution showed that B-site cations transferred from the main structure to the surface and were finally deposited into the metal or nanoparticles of alloy [73]. This process was able to signally boost the active site of the B ion on the surface, thus promoting the enhancement of the metal–oxide interface. Moreover, the reoxidation process in this process was reversible, so the catalyst agglomeration was likely to be avoided [74].

For the sake of further understanding the theory of Co dopants, Co-doped $Pr_{0.5}Ba_{0.5}MnO_{3-d}$ (PBMCO) was studied in the phase transformation as well as in the upstream and downstream phases by Kim et al. [51] Experimental results indicated that the doped one for CO oxidation had lower catalytic activity than ex-solved Co nanoparticles. Co@L-PBMCO had better adsorption capacity abilities of CO and was easier to format OVs and another activated surface.

Kwon et al. [75] made $LaCr_{0.95}Ir_{0.05}O_{3-\delta}$ catalyst and confirmed that the enhanced catalytic activity of it was based on the exsolution of Ir nanoparticles on the catalyst surface. The highest CH_4 conversion rate was 81%. When Ir was transferred to a perovskite surface with and without OVs, the heat release rate increased by 1.01 eV and 0.43 eV, respectively.

3.6. Etching Method

Plasma treatment was a workable method, as well as ion bombardment, for the formation of anionic defects in transition metal oxides by energetic ion or electron bombardment.

Peng et al. [45] studied that OVs in the catalyst of $LaFeO_3$ were produced by the way of plasma. Ar could regulate the concentration of OVs more easily than O_2. Experiments and calculations demonstrated that OVs improved the adsorption of weak hydroxyl groups and enhanced the performance of oxygen evolution. The production of a moderate concentration of OVs in $LaFeO_3$ was generated by the O_2-plasma.

Yang et al. [52] imported OVs and Co^{n+} Lewis acid sites into the ordered large pore size $La_{0.8}Sr_{0.2}CoO_3$ (LSCO) monomer catalyst and investigated their synergistic effects on methane combustion. Selecting oxalic acid one-step reduction and selective etching as the reaction method, the LSCO surface had higher coterminal sites, which induced the reduction in Co^{3+} to Co^{2+}, while producing Lewis acid active sites and OVs, because oxalate selectively etched Sr surface. The filled OVs and Lewis acid sites could boost the adsorption

capacity of methane, accelerating the catalytic combustion of methane. Additionally, having strong oxygen activation ability, lattice oxygen migration ability and reducibility was also the merits of this method. However, it should be noted that excessive OVs might be counterproductive to catalysis sometimes, so OVs should be regulated appropriately.

To sum up, choosing the appropriate method according to the requirements. Doping or substitution were common methods of introducing oxygen vacancies into transition metal oxides. Heat treatment could lead to the transformation of crystal structure and/or the exolysis of secondary active phase, thus comprehensively improving the activity of metal oxides. If a large number of OVs need to be generated without damaging the catalyst matrix structure in perovskite, plasma etching might be an excellent choice [76,77]. To avoid agglomeration of catalysts, exsolution could be selected.

4. Technologies for Detecting Oxygen Vacancies

OVs were able to alter the chemical, physical, and electronic properties of materials, so they became one of the most important research subjects. It was usually necessary to observe and analyze the phenomenon caused by OVs; however, due to their low concentration and short existence time, OVs were normally not visible to the naked eye. The relative concentration of OVs ranged from PPM to tens of atomic percent, a condition that was difficult to find a fitting experimental plan to characterize and distinguish OVs. Detecting specific concentrations of OVs was notoriously challenging. It was possible to probe OVs obliquely by the physical properties, such as microscopic form of matter or transition metal valence states, in a majority situations. A summary of these techniques is given in Table 3.

Table 3. Summary of technologies for detecting oxygen vacancies in perovskite.

Mathod	Ways to Detecting Oxygen Vacancies	Qualitative or Quantitative	Reference
X-ray diffraction (XRD)	Detect crystal structure and lattice parameters	Qualitative	[50,78,79]
X-ray photoelectron spectroscopy (XPS)	Elemental composition and chemical environment near the surface	Qualitative	[55,72,80]
Transmission electron microscopy (TEM) and scanning transmission electron microscopy (STEM)	Crystal structure and atomic arrangements	Qualitative	[81,82]
Raman spectra	A peak shift and/or the presence of additional peak	Qualitative	[49,78]
Ultraviolet-visible spectroscopy (UV-vis)	Peak changes	Qualitative	[76]
Thermogravimetric analysis (TGA)	Weight changes	Quantitative	[78,79]
X-ray Absorbtion Spectra (XAS), X-ray absorption fine structure (EXAFS) and X-ray absorption near-edge structure (XANES)	Variations of XAS peaks	Qualitative	[49,83]
Electron Paramagnetic Resonance (EPR)	Valuable information about unpaired electrons	Qualitative	[16,45,61,82]
H_2-TPR, O_2-TPD	Chemical absorption oxygen/the redox potential	Qualitative	[16,84]
Iodometric titration (IT)	Quantitative analysis oxygen Stoichiometry	Quantitative	[85,86]
Photoluminescence (PL) Spectroscopy	Electronic structure	Qualitative	[87,88]
Electron energy-loss spectroscopy (EELS)	Content and electronic structures	Qualitative	[25,89]
Neutron powder diffraction (NPD)	Crystal structures	Qualitative	[82,90]

4.1. Spectral Detection Methods

Thinking over the kinds of constraints in each technique, it was sometimes not convincing to prove the existence of OVs with just one technique. In the early research, various electron microscopes and radiation instruments, such as UV-vis and XRD, were used to characterize OVs in perovskite. In recent years, more advanced techniques that included HRTEM and EELs were used to characterize and gain insight into OVs in perovskite catalyst.

4.1.1. X-ray Photoelectron Spectroscopy (XPS)

X-ray photoelectron spectroscopy (XPS). It was one of the most important characterization techniques for analyzing OVs, which was characterized by the difference in the atomic number ratio of metal ions to lattice oxygen. XPS and others were employed together to analyze the structures of perovskites and concentrations of OVs. TiO_2 was obtained with distinctive concentrations of OVs by synthesizing a series of TiO_2 samples with different Cu-doping concentrations by Liang et al. [91]. Although pure TiO_2 could not absorb the visible light, UV-vis diffuse reflectance spectroscopy could easily detect the presence of OVs in TiO_2 samples. As the copper-doping concentration climbed, the intensity of absorption in the visible area increased, which led to the remarkable rising of the concentration of OVs (Figure 3a). More information about OVs in Cu-doped TiO_2 samples was displayed in the O 1s XPS (Figure 3b–e). By curve fitting, O 1s area precisely showed three peaks, which corresponded to lattice oxygen, surface hydroxyl oxygen, and adsorbed oxygen. They were located at 529.5, 530.5, and 531.5 eV.

Magray et al. [92] used a solid–state method and a laser deposition method to prepare La_2CoMnO_6 bulk (LCMO-B) and La_2CoMnO_6 films (LCMO-F), respectively. For the purpose of detecting OVs in the above two perovskites, rapid responding XPS measurements were performed. Figure 3f,g illustrates the Mn 2p XPS spectrum of LCMO-B and LCMO-F, respectively. Firstly, the background was used for the best fit, and then the normalized spectrum was used to figure out the charge states of Mn ions. Mn^{4+}, Mn^{3+}, and Mn^{2+} peaks were fitted to the Mn 2p 3/2 peak. Manganese in the sample was present in the Mn^{2+} state because of the satellite peak at 647.9 eV. This confirmed the presence of OVs in these samples. However, the peak intensity of Mn^{3+} and Mn^{2+} in LCMO-F was higher than that in LCMO-B, indicating that LCMO-F had more OVs. XPS detection technology could reflect the presence of OVs from the side, rather than directly detect the concentration.

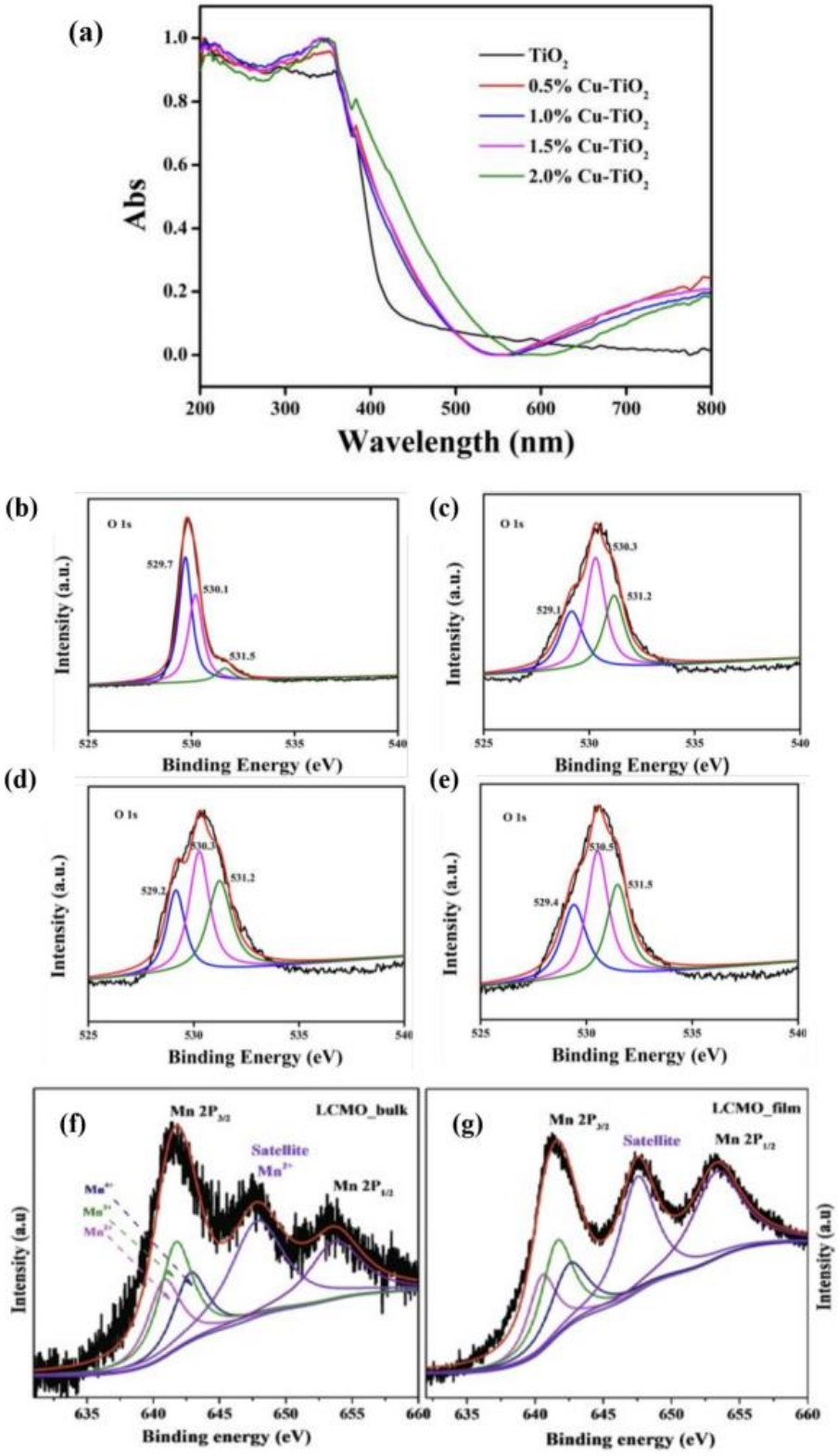

Figure 3. (**a**) UV-vis diffuse reflectance spectra of TiO_2 samples with different Cu loadings, XPS spectra of O 1s on the surface of (**b**) TiO_2, (**c**) 0.5% Cu-doped TiO_2, (**d**) 1.5% Cu-TiO_2, and (**e**) 2.0% Cu-doped TiO_2 samples, and XPS spectra of Mn 2p core level of (**f**) LCMO bulk and (**g**) LCMO film [91,92].

4.1.2. Raman Spectroscopy

Raman spectroscopy was widely applied in studying various defects, such as OVs caused by ion doping and so on, because the characterization method was high-efficiency and sensitive to the structure and bond order of perovskites [93]. For example, the chemical coordination structures of Pt/Nb_2O_5-AR_{10} (PNO-A) and Pt/Nb_2O_5-air (PNO-a) were studied by Raman spectroscopy. The peaks after several times magnification are shown Figure 4a,b. It could be clearly seen that in PNO-A, the peak concentrated at 685 cm^{-1}, while the peak of PNO-a shifted to 676 cm^{-1}, which could generate more OVs under Ar reaction.

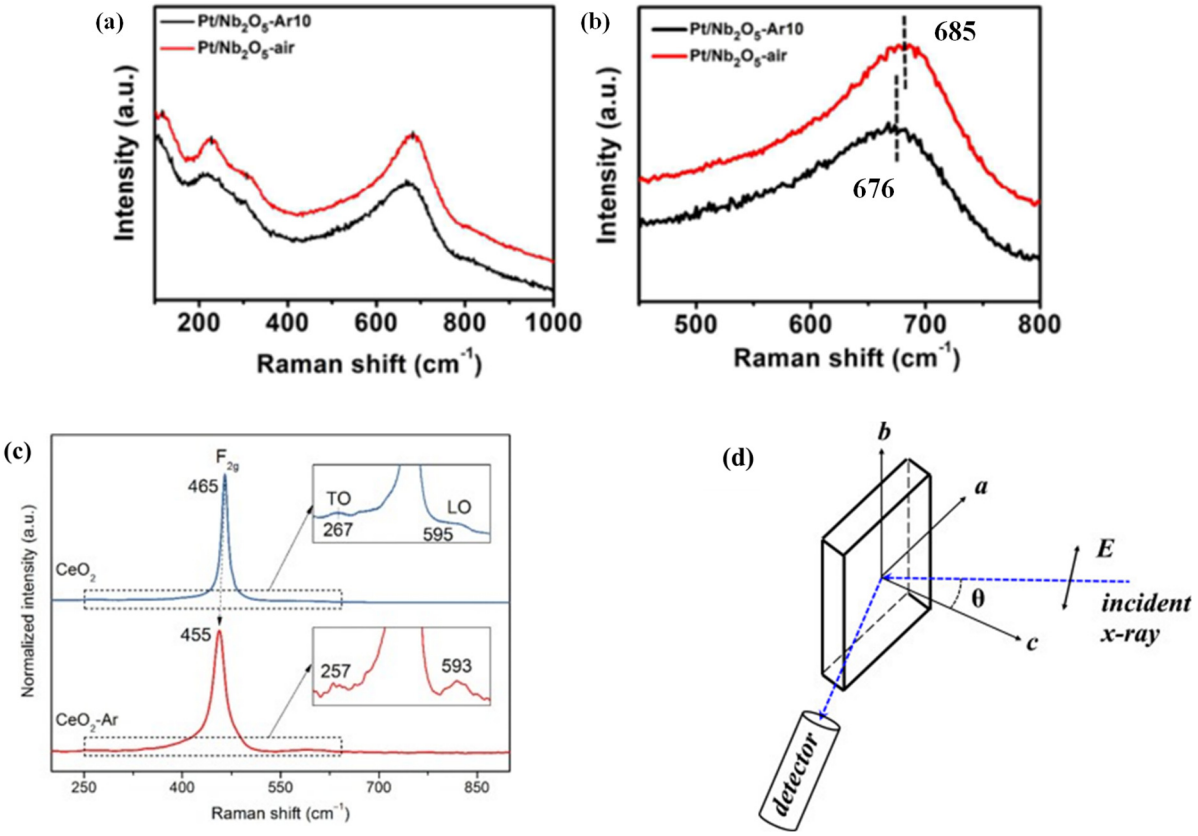

Figure 4. (**a**) Raman spectra of the representative Pt–based catalysts and (**b**) magnification of the peaks located at 450–800 cm^{-1}. (**c**) Raman spectra of the CeO_2 and CeO_2-Ar catalysts. (**d**) Schematic diagram of the polarized EXAFS measurement geometry [93–96].

The influence of OVs on NO selective reduction by CeO_2 was also investigated. Zhang et al. [94] found that the OV of CeO_2 roasted in the Ar atmosphere was higher than that of the roasting in ambient air. Figure 4c illustrates the Raman spectra of the two catalysts. Usually, the strain and the defect in the lattice caused the Raman band position and shape of the F2g mode at 465 cm^{-1}. The F2g oscillation frequency of the CeO_2-AR catalyst was changed to 455 cm^{-1}. The sample was calcined at 600 °C and then cooled to room temperature. Therefore, no residual strain was found in the lattice of CeO_2. Therefore, the inferred Raman band position shift might indicate that there were OVs in CeO_2-AR.

4.1.3. The X-ray Absorption Microstructural Spectrum (XAFS)

XAFS was developed on the basis of synchrotron radiation. The excited photoelectrons were dispersed by the surrounding atoms as X-rays passed through a sample, which resulted in an energy oscillation. The local electronic and geometric formation of the detected specimen could be obtained by detecting these oscillatory indicators [95].

The location of OVs of $Sr_2CuO_{3+\delta}$ was developed in a high-temperature superconductor by polarized extended X-ray absorption fine structure (EXAFS) by Wang et al. [96] The characterization analysis was that OVs were distributed in the material plane and apical position, about 10% and 8%, respectively. By rotating $Sr_2CuO_{3+\delta}$ around the b axis, polarized EXAFS at different incident angles was collected (Figure 4d), and the DFT was used in the calculation.

Xie et al. [97] used EXAFS to collect the information of $SrTiO_3$ (STO) doped with NiP. They concluded that the ratio of OVs in NiP/STO-60 was the highest among all samples; then, the order of oxygen octahedron structure was affected. The STO doped with NiP could gently adjust the relative concentrations of OVs, lattice oxygen, and adsorbed oxygen and significantly improve the catalytic hydrogen evolution activity due to the oxygen balance.

4.2. Electron Paramagnetic Resonance

EPR was a kind of magnetic resonance technology that could be used to detect the unpaired electrons contained in atoms or molecules of matter qualitatively and quantitatively. Then, the structural properties of the surrounding environment could be explored. Jing et al. [98], respectively, synthesized $LaFeO_3$ (LFO) and 3D micron globular $LaCo_{0.5}Fe_{0.5}O_3$ (LCFO) by the hydrothermal method. Both of these perovskites were used to activate PMS to degrade BPA, and the electron spin resonance (ESR) spectra of the two were compared to detect OVs (Figure 5a). LCFO exhibited stronger signal intensities due to electron capture sites on OVs. The peak intensity was proportional to the concentration of OVs, which also indicated that there were more OVs in the LCFO material. OVs in LCFO could be increased by ion co-doping in a LFO structure, thereby enhancing the activation ability of PMS [99].

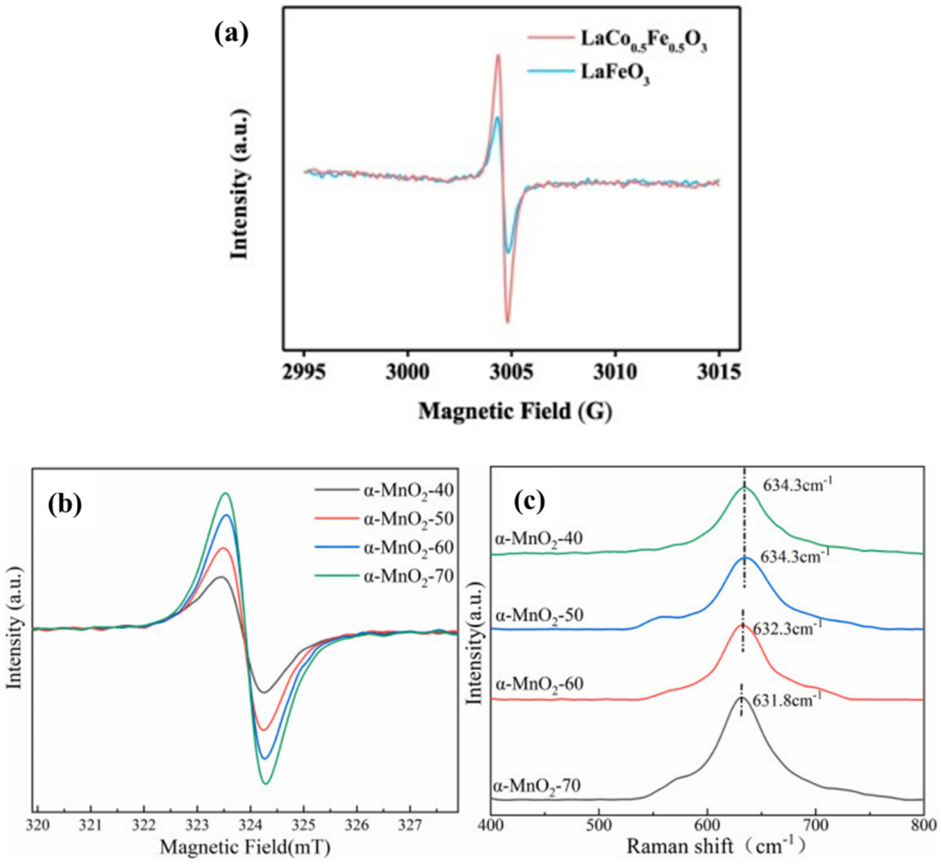

Figure 5. (**a**) $LaCo_{0.5}Fe_{0.5}O_3$ in $LaCo_{0.5}Fe_{0.5}O_3$/PMS system and ESR spectra representing oxygen vacancies in $LaFeO_3$ and $LaCo_{0.5}Fe_{0.5}O_3$ and EPR (**b**) and Raman (**c**) profiles of different catalysts [98–100].

The OVs in the various prepared MnO_2-x catalysts were characterized by EPR [100]. Electron delocalization on OVs might result in more symmetric signal peaks. As can be seen from Figure 5b,c, each catalyst had a symmetric EPR signal peak, indicating that there were certain OVs in each material. The changing trend of the signal peak intensity of different catalysts was as follows: MnO_2-1.8 (I_{peak} = 795) > MnO_2-2.0 (I_{peak} = 758) > MnO_2-1.65 (I_{peak} = 578) > MnO_2-1.5 (I_{peak} = 333) > MnO_2-1.8R (I_{peak} = 226). The content of OVs was directly reflected by the signal peak strength. When x = 1.8 in the prepared MnO_2-x sample, the signal strength of the catalyst was the strongest, suggesting that the MnO_2-1.8 catalyst had the highest OVs' concentration. Conversely, when x = 1.8R, the signal strength of the catalyst was the lowest, which indicated that it possessed the least amount of OVs [101].

Yang et al. [102] utilized EPR to probe into the hydrothermal α-Fe_2O_3 film and explored the kinetic and thermodynamic properties of its photoanodes in the presence or absence of OVs, understanding the effect of OVs on the water oxidation of the film. The consequence was that the film had an obvious EPR signal. Along with the time of hydrothermal treatment, the signal intensity of the material strengthened, indicating the increase in OVs.

4.3. Kelvin Probe Force Microscope and Electron Microscopy

The Kelvin probe force microscope (KPFM) was one of the most widely used instruments, which was susceptive to detect the concentrations of local OVs. The electronic characterization of semiconductor surfaces also could be performed by it. The preparation of $BiFeO_3$ (BFO) and hydrogenated BFO (HB-180-2-8) on the ITO surface was measured simultaneously with KPFM, respectively, and the morphology and CPD images are illustrated in Figure 6a,b. The variation of CPD cross-section variation values (ΔVCPD) was ~40 mV and ~140 mV, respectively, which were the original BFO and the hydrogenated BFO (HB-180-2-8); both them were clearly marked in CPD images with the marks of one, two, and three. The surface potential of unhydrogenated BFO nanocrystals was less than negative than that of hydrogenated BFO nanocrystals. The large number of OVs on the particle surface was due to the surface potential with a more negative shift of hydrogenated BFO, and these OVs could be used as active sites for electron capture [103]. The BFO particle electronic structure surface was actually altered by the use of a hydrogenation method in the image of KPFM. In an effort to better study the distribution and kinetics of OVs in $NdBaCo_2O_{5.5}$, the oxygen ions and their occupied positions were analyzed by means of neutron powder diffraction (NPD) and annular dark-field scanning transmission electron microscopy (ADF-STEM). A schematic diagram of the crystal structure of $NdBaCo_2O_{5.5}$ ($NBCO_{5.5}$) in TEM image is shown in Figure 6c. The image could be used to distinguish OVs and positions of oxygen atoms by the way of improving spatial resolution. Figure 6d displays the ordered arrangement of OVs' channels in the ND-O layer due to alternating the CoO_5 square cone and CoO_6 octahedron along the B-axis. ADF-STEM image simulation was carried out on the measured grid parameters and the optimized DFT model in order to demonstrate the experimental results. The image showed that OVs' channels were empty, and the atomic columns of Nd, Ba and Co were murky, which was consistent with the experimental image primely [104].

Yang et al. [105] prepared a series of doped $Mn_xZr_{1-x}O_2$ catalysts by partially substituting tetravalent zirconium in ZrO_2 with low-valent manganese dopants (Mn^{2+}). The conclusion was the Mn heteroatom could be introduced into the zirconia lattice and partially replaced for the zirconia. It could be seen from the lattice parameter diagram (Figure 6e,f) that changing Zn with a small ionic radius to Mn with a large ionic radius led to lattice expansion and a decrease in lattice parameters. The Kring–Vink notation demonstrated that the replacement of heteroatoms with lower valence could induce the appearance of negatively charged defects (Mn''_{Zr}) and OVs:

$$Mn^{2+} \overset{ZrO_2}{\rightarrow} Mn''_{Zr} + V_O^{\cdot\cdot} \quad (2)$$

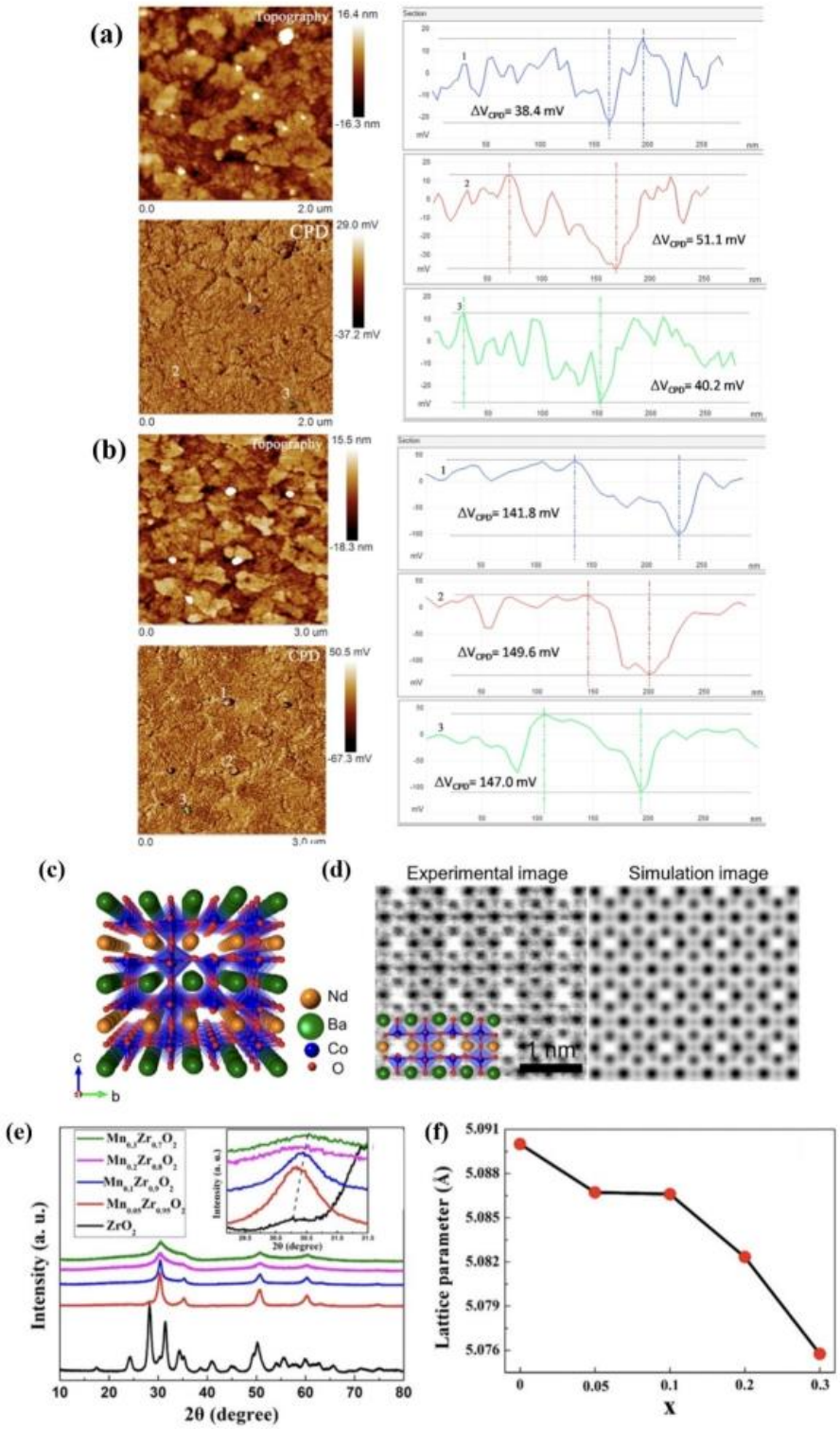

Figure 6. Topography and contact potential difference (CPD) images of as-prepared (**a**) BFO and (**b**) hydrogenated BFO (HB−180−2−8) nanoparticles on ITO surface measured by KPFM. The cross−se−tional line profiles of CPD are achieved along the lines indicated by numbers 1, 2, and 3 in CPD images and direct observation of oxygen vacancy channels in $NdBaCo_2O_{5.5}$ ($NBCO_{5.5}$) double perovskite. (**c**) Schematic view of the structure of $NBCO_{5.5}$. (**d**) ADF STEM and simulated images of $NBCO_{5.5}$ taken in the [100] zone axis. (**e**) HAADF image of $NBCO_{5.5}$ with the EDS elemental map of Nd, Ba, and Co. (**f**) XRD patterns of $MnxZr_{1-x}O_2$ catalysts [103–105].

It was confirmed that the addition of Mn_2 ions into a ZrO_2 lattice could lead to a large amount of OVs, which was probably one of the causes of the reduction in lattice parameters.

4.4. H_2-TPR, O_2-TPD

Temperature programmed desorption (TPD) was a technique used to measure the surface properties of an active center. Temperature programmed reduction (TPR) could measure the reducibility of a substance. $La_{0.9}K_{0.1}CoO_3/ZrO_2$ (LKC/Z), $LaFeO_3/ZrO_2$ (LF/Z), and pure $LaFeO_3$ (Pure-LF) were prepared by Guo et al. [106] The TPR profiles of all samples are shown in Figure 7a. The reduction in Fe^{4+} to Fe^{3+} occurred in two places: one was a small H_2 consumption peak of LF/Z material at around 370 °C, and the other was a relatively obvious H_2 consumption peak, which appeared in the sample of x = 0.2. Another significant H_2 consumption peak appeared in the x = 0.1 sample due to the reduction in Co^{3+} to Co^{2+} at low temperature. The reduction in the above metal ions led to the formation of OVs on the surface of perovskite. The O_2-TPD spectra (Figure 7b) of CuO and $La_2CuO_{4-\delta}$ (LCO) showed LCO had more surface chemisorbed oxygen because several of the main low-peak strengths of CuO were less than LCO at 800 °C [107].

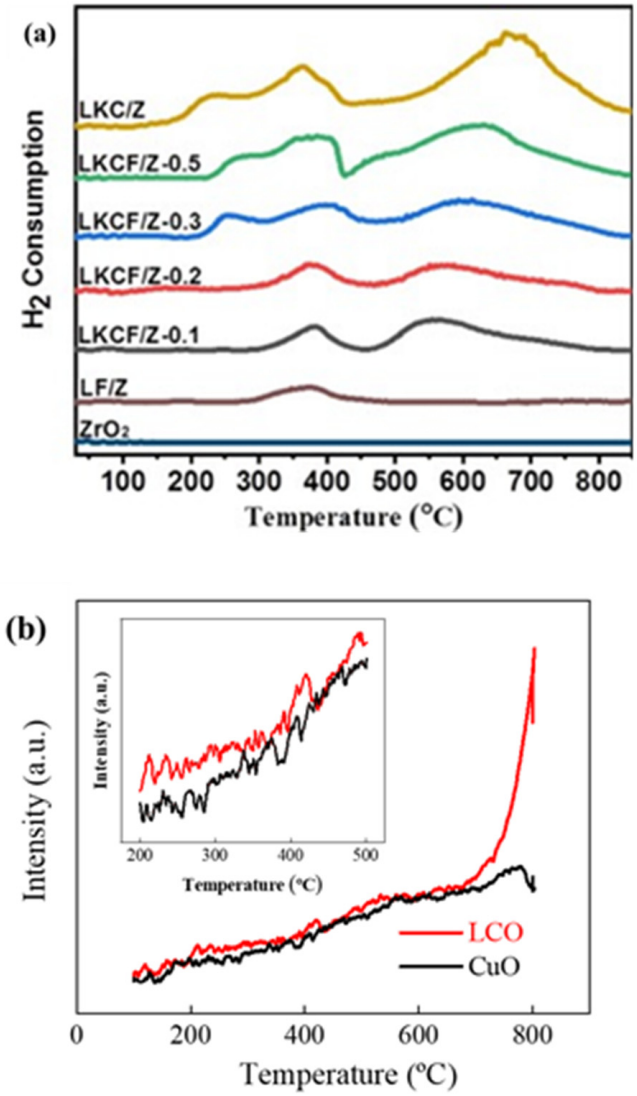

Figure 7. (**a**) The TPR profiles of LKCF/Z-x (x = 0.1–0.3 and 0.5), LKC/Z, LF/Z and ZrO_2 after calcination [106] and (**b**) O_2-TPD profiles of LCO and CuO [107].

4.5. Gravimetric Method

The gravimetric method was the way to determine the component content of the measured substance by weighing the mass of the substance. For the purpose of quantitatively studying the OVs' concentration, the OVs-rich α-Fe_2O_3 was obtained by the gravimetric method. Three specimens were prepared on the basis that the molar ratios of α-Fe_2O_3 and tartaric acid were, respectively, 1/5, 1/7, and 1/10, expressed as S1, S2, and S3. The OVs-rich sample, in which mv was 1000 mg, was transformed into an OVs-free sample (m_o) after oxygen annealing at 400 °C for 2 h.

The concentration of OVs (%) was calculated by the Equations (3) and (4):

$$\Delta m = m_o - m_v \tag{3}$$

$$OVs\% = 10/3(\Delta m - \Delta m_x)/m_v \times 100\% \tag{4}$$

where Δm_x was the evaporation of α-Fe_2O_3 at 400 °C, and the weight of absorbed water was calibrated by repeated blank tests.

In the absence of OVs, the mean weight loss of α-Fe_2O_3 (Δm_x) was −3.4. For OVs-rich α-Fe_2O_3 (Δm), S2 and S3 were, respectively, +1.4 mg and −2.0 mg. As a result, S2 and S3 had an OVs mass ($\Delta m - \Delta m_x$) of +4.8 mg and +1.4 mg. Then, in accordance with Equation (2), S3 and S2 were calculated to be 1.6% and 0.4%, respectively. The results for S1 and S4 were not clear, mainly due to the fact that they were too low to weigh (<0.1%), which exceeded the capacity of the device [90]. Other methods for the quantitative detection of OVs according to different concentrations were also studied [36].

5. Reduction Mechanism of Oxygen Vacancies

5.1. Roles of Oxygen Vacancies in the ROS

AOPs was mainly marked by the production of •OH, which had the strong redox potential [108]. In addition to the production of hydroxyl radicals, AOPs also produced other reactive oxygen species (ROS), such as $SO_4^{\bullet -}$, O_2^-, H_2O_2, $^1O_2$, O_3, and so on [109,110]. The presence of OVs could improve the reactivity of ROS. These reactive species triggered a series of free radical chain reactions that attack organic pollutants and thus purify them.

Here are the equations for the reaction of hydroxyl radicals with organic compounds:

$$HO\bullet + R\text{-}H \rightarrow H_2O + R\bullet \tag{5}$$

$$HO\bullet + C{=}C \rightarrow HO\text{-}C\text{-}C\bullet \tag{6}$$

$$HO\bullet + Ph\text{-}H \rightarrow Ph\text{-}H(OH)\bullet \tag{7}$$

Yang et al. [111] made various perovskite catalysts with an $A_{n+1}BnO_{3n+1}$-RP structure to efficiently catalyze phenol degradation. OVs had high activity and mobility, which could promote the generation of PMS free radicals. Reasonable adjustment of OVs in catalysts could maximize the singlet oxygen pathway. OVs on perovskite catalysts activated high-energy oxidants into ROS, which could easily attack organic wastes, break chemical bonds, and achieve rapid degradation of pollutants.

5.2. Evaluation of the Catalytic Activity of Oxygen Vacancies

In view of the importance of OVs in ROS, the need to evaluate it was raised. Based on the above detection system, further qualitative and quantitative evaluation through theoretical calculation could improve the accuracy of the study. Understanding the characteristics of OVs at the macro and micro levels, respectively, was very beneficial for evaluating the catalytic performance of perovskites and designing better catalyst materials. Although the various detection techniques mentioned in part 4 were useful tools for evaluating OVs, their combination with theoretical calculations or models would provide a deeper insight

into the reaction principle. Then, the first-principles calculations were presented to evaluate OVs with other techniques.

Principle was a technical term for computational physics or computational chemistry. The broad term first-principles computation referred to all calculations based on the principles of quantum mechanics. First-principles calculations recognized physical and other properties of materials from the scale of the atoms and electrons. The traditional continuum theory focused more on the movement of ions in matter, which was based on the adiabatic principle. However, the effect and action of electrons actually were present in the matter that was neglected. Electron charge as the medium of particle motion was the most important research object in first-principles calculation. The method called first-principles calculation did not need any additional parameters, as long as the basic constitution conditions of molecular structure and matter were known. This theory was close to the principle reflecting the basic nature of the universe. The first principle included two major categories, one was ab initio calculation, and the other was the DFT calculation. Ab initio was a first-principles calculation in a narrow sense. It referred to a quantum calculation using a little bit of data in the experiment instead of empirical parameters. However, this calculation was very slow, so adding some empirical parameters could greatly speed up the calculation, while inevitably sacrificing the accuracy of the calculation results. The first principle was a very effective tool for calculating the microstructure and properties of materials, especially crystalline materials.

DFT was the indispensable and important theory in the calculation of electronic structure and total energy of the system. DFT included Thomas–Fermi–Dirac (T–F–D) approximation, Hohenberg–Kohn (H–K) theorem, GGA (generalized gradient approximation), and other commutative correlation functional approximation equations [112]. First-principles computing software included Materials Studio (MS), and MS integrated multiple time and spatial scales. The simulation method could be realized from microscopic electronic structure to macroscopic performance prediction. The cross-scale scientific study of measurement was the current relative in the field of molecular simulation. Accurate, stable, and efficient material simulation software for commercial computing Materials Visualizer is the core, mainly including CASTEP, $DMol_3$, Forcite$^+$, COMPASS, 22 modules in total. In addition, the calculation software also included Vienna AB Initio Simulation Package (VASP), WIEN series, WinXMorph, VESTA (Visualization for Electronic and Struc-) Tural Analysis program, Band, Gaussian98 program package, PWSCF (Plane-Wave self-consistent field), Crystal, and other programs.

The double perovskite Sr_2FeMoO_6 studied the electronic and other properties of OVs by first-principles [113]. There, XAS and XMCD showed a better agreement with experimental spectra than with previous density functional calculations. This indicated that the experimentally observed mixed valency of the Fe ion (Fe^{2+} or Fe^{3+}) was mainly caused by OVs.

The $LaAlO_3/KTaO_3$ heterostructure (HS) was reported, and the formation energy of OVs in HS was demonstrated using first-principles density functional theory calculations [114]. They calculated the HS models with OVs at different positions and calculated the OVs' formation energy.

The formation energy of OVs in O-rich and O-poor regions was illustrated (Figure 8) The lower formation energy was observed at the interface $(TaO_2)^+$ layer and the surface $(LaO)^+$ layer. It was found that OVs were easier to form at the interface $(TaO_2)^+$ and $(LaO)^+$ layer. Here, they studied the formation and migration of oxygen vacancies in $YMnO_3$ using DFT calculations. They found a strong preference for the formation of vacancies at the planar O_4 sites in bulk, which were not trimerization centers. Oxygen vacancies migrated most easily in the Mn-O layers between O_4 sites.

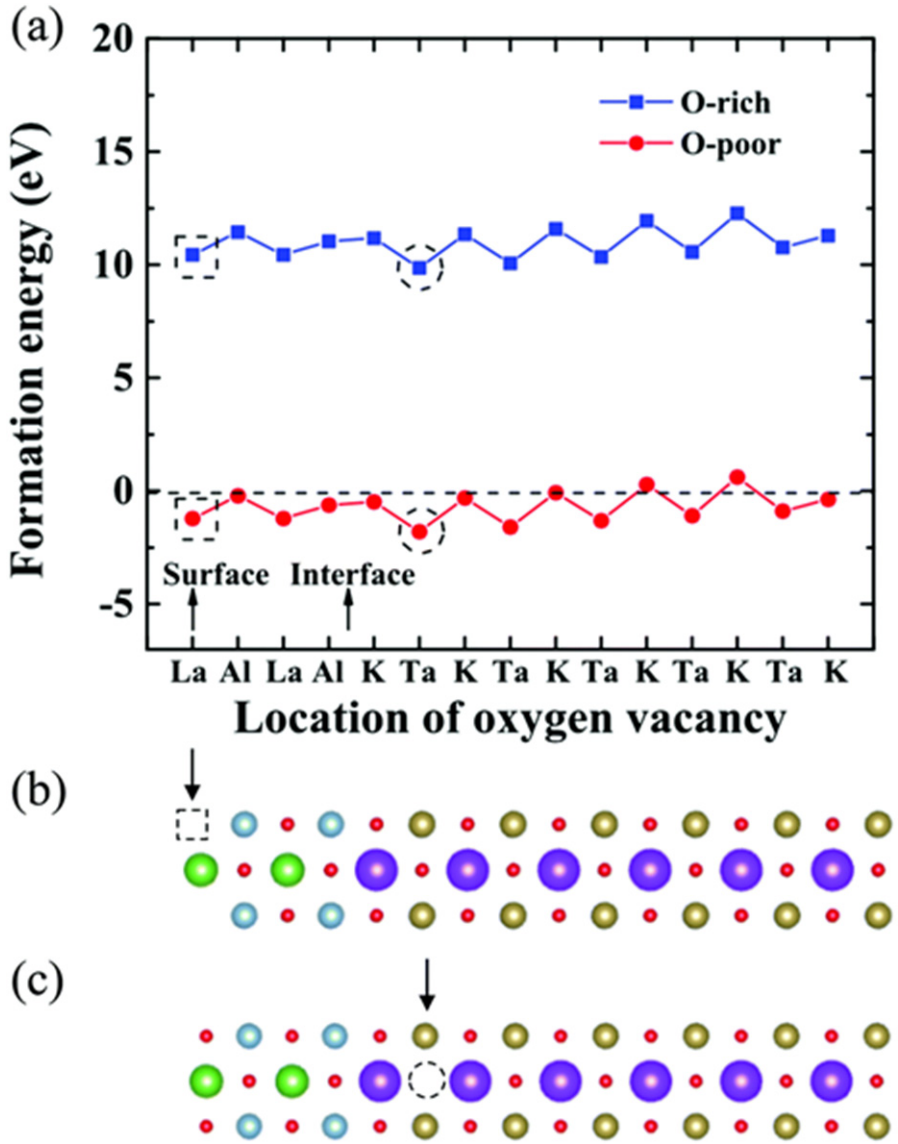

Figure 8. (**a**) Calculated formation energies of oxygen vacancies at different atomic layers in the p-type $LaAlO_3/KTaO_3$ under O−rich and O−poor conditions, respectively. Atomic layers of $(KO)^-$, $(TaO_2)^+$, $(LaO)^+$, and $(AlO_2)^-$ are denoted as K, Ta, La, and Al, respectively. (**b**) Partial side view of the $LaAlO_3/KTaO_3$ HS-based slab model with an oxygen vacancy on the surface marked by a square. (**c**) Partial side view of the $LaAlO_3/KTaO_3$ HS-based slab model with an oxygen vacancy on the TaO_2 layer near the interface marked by a circle [114].

6. Conclusions and Perspectives

This review introduced the methods to improve OVs in perovskites, the strategies to detect OVs, and the role of OVs in the kinds of AOPs. The method of regulating OVs and advanced characterization techniques in perovskite played a vital role in a number of proceeding research fields. In order to better understand and interpret the experimental results, the relevant theoretical calculation and DFT model provided indispensable theoretical and technical support, as well as provided guidance information for the design of catalysts and the study of a reaction mechanism. Although perovskite was used as an example to explain the influence of OVs on catalyst degradation in this paper, the OV manufacturing technology and the detection method described herein could also be applied to many other material systems.

According to the current research status of OVs in perovskites, the following suggestions were put forward for future research direction:

(1) Although the importance of OVs was gradually realized, and the regulation and detection techniques of OVs were developed, more and more challenges could not be ignored. In the first place, it was urgent and necessary to develop more precise and convenient devices for producing OVs in a green and an efficient way. In the second place, a new controlled method for the generation of OVs could be found. In order to improve the stability of OVs, it was necessary to precisely quantify the OVs and determine their actual location, even providing a reference scheme for the study of other catalytic materials. Last but not least, the research on other defects of the catalyst could be helpful in understanding the mechanism of OVs, which could be used to design more efficient catalysts and surge the degradation of pollutants.

(2) In order to reasonably design high-performance perovskite catalysts, it was necessary to obtain more information about the mechanism of the influence of OVs on perovskite activity. Therefore, research should combine experimental methods with more advanced theoretical analysis or models. Theoretical calculation could clarify the reaction path in the presence of OVs, and models were the tool for rapid mechanism analysis. By combining the resulting OVs from model or theoretical calculations with various experimental representations, the role of OVs in terms of activity could be better understood.

(3) More precise regulation of OVs' concentrations and detection of small amounts of OVs were challenging. Some regulatory technologies of OVs faced problems, including aggregation of catalyst materials, high requirements for instruments, poor stability, etc. Therefore, there were many technical difficulties in how to accurately control the regulation effect of OVs in perovskite and how to apply the regulation method to practical production. These were also important issues that must be paid attention to during the study of OVs.

Author Contributions: Writing—original draft preparation, J.Y.; conceptualization, H.L.; methodology, N.L., resources, Y.G. and J.C., supervision, H.J., writing—review and editing, Y.W. and X.Z. All authors have read and agreed to the published version of the manuscript.

Funding: This research was funded by National Natural Science Foundation of China grant number 42177269, 12175132, 21806107.

Data Availability Statement: All individuals included in this section have consented to the acknowledgement.

Acknowledgments: This work was sponsored financially by National Natural Science Foundation of China (No. 42177269, 12175132, 21806107).

Conflicts of Interest: The authors declare no conflict of interest.

References

1. Urán, L.; Gallego, J.; Li, W.-Y.; Santamaría, A. Effect of catalyst preparation for the simultaneous removal of soot and NOx. *Appl. Catal. A* **2019**, *569*, 157–169. [CrossRef]
2. Liu, N.; Dang, Y.; Hu, B.; Tian, M.; Jiang, H.; Quan, G.; Qiao, R.; Lei, J.; Zhang, X. BN/Fe3O4/MIL-53(Fe) ternary nanocomposite for boosted ibuprofen degradation by visible light assisted photocatalytic activation of persulfate. *Surf. Interfaces* **2022**, *35*, 102472. [CrossRef]
3. Chen, Y.-D.; Duan, X.; Zhou, X.; Wang, R.; Wang, S.; Ren, N.-Q.; Ho, S.-H. Advanced oxidation processes for water disinfection: Features, mechanisms and prospects. *Chem. Eng. J.* **2021**, *409*, 128207. [CrossRef]
4. Yang, Y.; Gu, Y.; Lin, H.; Jie, B.; Zheng, Z.; Zhang, X. Bicarbonate-enhanced iron-based Prussian blue analogs catalyze the Fenton-like degradation of p-nitrophenol. *J. Colloid Interface Sci.* **2022**, *608*, 2884–2895. [CrossRef] [PubMed]
5. Wang, Y.; Wang, R.; Lin, N.; Xu, J.; Liu, X.; Liu, N.; Zhang, X. Degradation of norfloxacin by MOF-derived lamellar carbon nanocomposites based on microwave-driven Fenton reaction: Improved Fe(III)/Fe(II) cycle. *Chemosphere* **2022**, *293*, 133614. [CrossRef] [PubMed]
6. Lin, N.; Gong, Y.; Wang, R.; Wang, Y.; Zhang, X. Critical review of perovskite-based materials in advanced oxidation system for wastewater treatment: Design, applications and mechanisms. *J. Hazard. Mater.* **2022**, *424*, 127637. [CrossRef]
7. Zhang, X.; Yue, K.; Rao, R.; Chen, J.; Liu, Q.; Yang, Y.; Bi, F.; Wang, Y.; Xu, J.; Liu, N. Synthesis of acidic MIL-125 from plastic waste: Significant contribution of N orbital for efficient photocatalytic degradation of chlorobenzene and toluene. *Appl. Catal. B* **2022**, *310*, 121300. [CrossRef]

8. Yang, Y.; Ji, W.; Li, X.; Lin, H.; Chen, H.; Bi, F.; Zheng, Z.; Xu, J.; Zhang, X. Insights into the mechanism of enhanced peroxymonosulfate degraded tetracycline using metal organic framework derived carbonyl modified carbon-coated Fe0. *J. Hazard. Mater.* **2022**, *424*, 127640. [CrossRef]
9. Yang, Y.; Zhao, S.; Bi, F.; Chen, J.; Li, Y.; Cui, L.; Xu, J.; Zhang, X. Oxygen-vacancy-induced O2 activation and electron-hole migration enhance photothermal catalytic toluene oxidation. *Cell Rep. Phys. Sci.* **2022**, *3*, 101011. [CrossRef]
10. Pan, Q.; Gao, Q.; Gao, G.; Liu, M.; Han, B.; Xia, K.; Zhou, C. Composition-engineered LaCoO3-based monolithic catalysts for easily operational and robust peroxymonosulfate activation. *Chem. Eng. J.* **2021**, *424*, 130574. [CrossRef]
11. Gao, P.; Yan, S.; Tian, X.; Nie, Y.; Wang, Y.; Deng, Y.; Tu, J. Identification and manipulation of active centers on perovskites to enhance catalysis of peroxymonosulfate for degradation of emerging pollutants in water. *J. Hazard. Mater.* **2022**, *424*, 127384. [CrossRef] [PubMed]
12. Jing, Y.; Aluru, N. The role of A-site ion on proton diffusion in perovskite oxides (ABO3). *J. Power Sources* **2020**, *445*, 227327. [CrossRef]
13. Rischau, C.W.; Lin, X.; Grams, C.P.; Finck, D.; Harms, S.; Engelmayer, J.; Lorenz, T.; Gallais, Y.; Fauqué, B.; Hemberger, J.; et al. A ferroelectric quantum phase transition inside the superconducting dome of $Sr_{1-x}Ca_xTiO_{3-\delta}$. *Nat. Phys.* **2017**, *13*, 643–648. [CrossRef]
14. Xiong, J.; Di, J.; Xia, J.; Zhu, W.; Li, H. Surface Defect Engineering in 2D Nanomaterials for Photocatalysis. *Adv. Funct. Mater.* **2018**, *28*, 1801983. [CrossRef]
15. Geng, G.; Cai, M.; Fang, R.; Luan, Q.; Zhang, Z.; Song, J.; Zhang, J. Metal-organic frameworks-derived perovskite catalysts for efficient degradation of 2, 4-dichlorophenol via peroxymonosulfate activation. *Appl. Surf. Sci.* **2020**, *534*, 147467. [CrossRef]
16. Chen, H.; Xu, Y.; Zhu, K.; Zhang, H. Understanding oxygen-deficient La2CuO4-δperovskite activated peroxymonosulfate for bisphenol A degradation: The role of localized electron within oxygen vacancy. *Appl. Catal. B* **2021**, *284*, 119732. [CrossRef]
17. Wang, Y.; Wang, J.; Du, B.; Wang, Y.; Xiong, Y.; Yang, Y.; Zhang, X. Synthesis of hierarchically porous perovskite-carbon aerogel composite catalysts for the rapid degradation of fuchsin basic under microwave irradiation and an insight into probable catalytic mechanism. *Appl. Surf. Sci.* **2018**, *439*, 475–487. [CrossRef]
18. Palas, B.; Ersöz, G.; Atalay, S. Catalytic wet air oxidation of Reactive Black 5 in the presence of LaNiO3 perovskite catalyst as a green process for azo dye removal. *Chemosphere* **2018**, *209*, 823–830. [CrossRef]
19. Li, H.; Yu, J.; Gong, Y.; Lin, N.; Yang, Q.; Zhang, X.; Wang, Y. Perovskite catalysts with different dimensionalities for environmental and energy applications: A review. *Sep. Purif. Technol.* **2023**, *307*, 122716. [CrossRef]
20. Lin, H.; Jie, B.; Ye, J.; Zhai, Y.; Luo, Z.; Shao, G.; Chen, R.; Zhang, X.; Yang, Y. Recent advance of macroscopic metal-organic frameworks for water treatment: A review. *Surfaces Interfaces* **2023**, *36*, 102564. [CrossRef]
21. Tahini, H.A.; Tan, X.; Schwingenschlögl, U.; Smith, S.C. Formation and Migration of Oxygen Vacancies in $SrCoO_3$ and Their Effect on Oxygen Evolution Reactions. *ACS Catal.* **2016**, *6*, 5565–5570. [CrossRef]
22. Run, Z.; Hao, Y. Oxygen vacancies induced tuning effect on physical properties of multiferroic perovskite oxide thin films. *Acta Phys. Sin.* **2018**, *67*, 156101. [CrossRef]
23. Wang, K.; Han, C.; Shao, Z.; Qiu, J.; Wang, S.; Liu, S. Perovskite Oxide Catalysts for Advanced Oxidation Reactions. *Adv. Funct. Mater.* **2021**, *31*, 2102089. [CrossRef]
24. Chen, D.; Chen, C.; Baiyee, Z.M.; Shao, Z.; Ciucci, F. Nonstoichiometric Oxides as Low-Cost and Highly-Efficient Oxygen Reduction/Evolution Catalysts for Low-Temperature Electrochemical Devices. *Chem. Rev.* **2015**, *115*, 9869–9921. [CrossRef] [PubMed]
25. Yaremchenko, A.A.; Populoh, S.; Patrício, S.G.; Macías, J.; Thiel, P.; Fagg, D.P.; Weidenkaff, A.; Frade, J.R.; Kovalevsky, A.V. Boosting Thermoelectric Performance by Controlled Defect Chemistry Engineering in Ta-Substituted Strontium Titanate. *Chem. Mater.* **2015**, *27*, 4995–5006. [CrossRef]
26. Aidhy, D.S.; Liu, B.; Zhang, Y.; Weber, W.J. Chemical expansion affected oxygen vacancy stability in different oxide structures from first principles calculations. *Comput. Mater. Sci.* **2015**, *99*, 298–305. [CrossRef]
27. Luo, X.J.; Liu, Y.S.; Yang, C.P.; Chen, S.S.; Tang, S.L.; Bärner, K. Oxygen vacancy related defect dipoles in CaCu3Ti4O12: Detected by electron paramagnetic resonance spectroscopy. *J. Eur. Ceram. Soc.* **2015**, *35*, 2073–2081. [CrossRef]
28. Zhao, S.; Gao, L.; Lan, C.; Pandey, S.S.; Hayase, S.; Ma, T. Oxygen vacancy formation and migration in double perovskite Sr_2CrMoO_6: A first-principles study. *RSC Adv.* **2016**, *6*, 43034–43040. [CrossRef]
29. Jia, Y.; Miglio, A.; Gonze, X.; Mikami, M. Ab-initio study of oxygen vacancy stability in bulk and Cerium-doped lutetium oxyorthosilicate. *J. Lumin* **2018**, *204*, 499–505. [CrossRef]
30. Haeussler, A.; Abanades, S.; Jouannaux, J.; Julbe, A. Non-Stoichiometric Redox Active Perovskite Materials for Solar Thermochemical Fuel Production: A Review. *Catalysts* **2018**, *8*, 611. [CrossRef]
31. Li, J.; Wang, J.; Kuang, H.; Zhang, H.R.; Zhao, Y.Y.; Qiao, K.M.; Wang, F.; Liu, W.; Wang, W.; Peng, L.C.; et al. Oxygen defect engineering by the current effect assisted with temperature cycling in a perovskite-type $La_{0.7}Sr_{0.3}CoO_3$ film. *Nanoscale* **2017**, *9*, 13214–13221. [CrossRef] [PubMed]
32. Smith, E.; Škapin, S.; Ubic, R. Correlative models for oxygen vacancies in perovskites. *J. Alloy. Compd.* **2020**, *836*, 155475. [CrossRef]
33. Li, B.; Yang, Q.; Peng, Y.; Chen, J.; Deng, L.; Wang, D.; Hong, X.; Li, J. Enhanced low-temperature activity of LaMnO3 for toluene oxidation: The effect of treatment with an acidic KMnO4. *Chem. Eng. J.* **2019**, *366*, 92–99. [CrossRef]

34. Zhang, X.; Zhao, Z.; Zhao, S.; Xiang, S.; Gao, W.; Wang, L.; Xu, J.; Wang, Y. The promoting effect of alkali metal and H2O on Mn-MOF derivatives for toluene oxidation: A combined experimental and theoretical investigation. *J. Catal.* **2022**, *415*, 218–235. [CrossRef]
35. Du, X.; Li, C.; Zhao, L.; Zhang, J.; Gao, L.; Sheng, J.; Yi, Y.; Chen, J.; Zeng, G. Promotional removal of HCHO from simulated flue gas over Mn-Fe oxides modified activated coke. *Appl. Catal. B* **2018**, *232*, 37–48. [CrossRef]
36. Gunkel, F.; Christensen, D.V.; Chen, Y.Z.; Pryds, N. Oxygen vacancies: The (in)visible friend of oxide electronics. *Appl. Phys. Lett.* **2020**, *116*, 120505. [CrossRef]
37. Christensen, D.V.; Trier, F.; Niu, W.; Gan, Y.; Zhang, Y.; Jespersen, T.S.; Chen, Y.; Pryds, N. Stimulating Oxide Heterostructures: A Review on Controlling SrTiO $_3$ -Based Heterointerfaces with External Stimuli. *Adv. Mater. Interfaces* **2019**, *6*, 1900772. [CrossRef]
38. Pryds, N.; Esposito, V. When two become one: An insight into 2D conductive oxide interfaces. *J. Electroceramics* **2016**, *38*, 1–23. [CrossRef]
39. Zhao, S.; Yang, Y.; Bi, F.; Chen, Y.; Wu, M.; Zhang, X.; Wang, G. Oxygen vacancies in the catalyst: Efficient degradation of gaseous pollutants. *Chem. Eng. J.* **2023**, *454*, 140376. [CrossRef]
40. Bai, J.; Zhang, B.; Xiong, T.; Jiang, D.; Ren, X.; Lu, P.; Fu, M. Enhanced visible light driven photocatalytic performance of Bi2WO6 nano-catalysts by introducing oxygen vacancy. *J. Alloy. Compd.* **2021**, *887*, 161297. [CrossRef]
41. Wu, J.; Li, X.; Shi, W.; Ling, P.; Sun, Y.; Jiao, X.; Gao, S.; Liang, L.; Xu, J.; Yan, W.; et al. Efficient Visible-Light-Driven CO $_2$ Reduction Mediated by Defect-Engineered BiOBr Atomic Layers. *Angew. Chem. Int. Ed.* **2018**, *57*, 8719–8723. [CrossRef] [PubMed]
42. Wang, M.; Shen, M.; Jin, X.; Tian, J.; Li, M.; Zhou, Y.; Zhang, L.; Li, Y.; Shi, J. Oxygen Vacancy Generation and Stabilization in CeO_{2-x} by Cu Introduction with Improved CO_2 Photocatalytic Reduction Activity. *ACS Catal.* **2019**, *9*, 4573–4581. [CrossRef]
43. Chu, K.; Liu, F.; Zhu, J.; Fu, H.; Zhu, H.; Zhu, Y.; Zhang, Y.; Lai, F.; Liu, T. A General Strategy to Boost Electrocatalytic Nitrogen Reduction on Perovskite Oxides via the Oxygen Vacancies Derived from A-Site Deficiency. *Adv. Energy Mater.* **2021**, *11*, 2003799. [CrossRef]
44. Wang, Y.; Wang, R.; Yu, L.; Wang, Y.; Zhang, C.; Zhang, X. Efficient reactivity of LaCu0.5Co0.5O3 perovskite intercalated montmorillonite and g-C3N4 nanocomposites in microwave-induced H2O2 catalytic degradation of bisphenol A. *Chem. Eng. J.* **2020**, *401*, 126057. [CrossRef]
45. Peng, X.; Zheng, J.; Zhang, Y.; Wang, Z. Tuning oxygen vacancies on LaFeO3 perovskite as efficient electrocatalysts for oxygen evolution reaction. *Mater. Lett.* **2021**, *309*, 131317. [CrossRef]
46. Gu, W.; Wang, W.; Li, G.; Xie, H.; Wong, P.K.; An, T. Microwave-assisted synthesis of defective tungsten trioxide for photocatalytic bacterial inactivation: Role of the oxygen vacancy. *Chin. J. Catal.* **2020**, *41*, 1488–1497. [CrossRef]
47. He, L.; Zhang, Y.; Zang, Y.; Liu, C.; Wang, W.; Han, R.; Ji, N.; Zhang, S.; Liu, Q. Promotion of A-Site Ag-Doped Perovskites for the Catalytic Oxidation of Soot: Synergistic Catalytic Effect of Dual Active Sites. *ACS Catal.* **2021**, *11*, 14224–14236. [CrossRef]
48. Zhang, P.; Mei, X.; Zhao, X.; Xiong, J.; Li, Y.; Zhao, Z.; Wei, Y. Boosting Catalytic Purification of Soot Particles over Double Perovskite-Type $La_{2-x}K_xNiCoO_6$ Catalysts with an Ordered Macroporous Structure. *Environ. Sci. Technol.* **2021**, *55*, 11245–11254. [CrossRef]
49. Wei, Y.; Zheng, Y.; Hu, Y.; Huang, B.; Sun, M.; Da, P.; Xi, P.; Yan, C.-H. Controlling the Cation Exsolution of Perovskite to Customize Heterostructure Active Site for Oxygen Evolution Reaction. *ACS Appl. Mater. Interfaces* **2022**, *14*, 25638–25647. [CrossRef]
50. Pang, S.; Yang, G.; Jiang, X.; Shen, X.; Rao, D.; Chen, C. Insight into tuning the surface and bulk microstructure of perovskite catalyst through control of cation non-stoichiometry. *J. Catal.* **2020**, *381*, 408–414. [CrossRef]
51. Kim, K.; Joo, S.; Huang, R.; Kim, H.J.; Kim, G.; Han, J.W. Mechanistic insights into the phase transition and metal ex-solution phenomena of $Pr_{0.5}Ba_{0.5}Mn_{0.85}Co_{0.15}O_{3-\delta}$ from simple to layered perovskite under reducing conditions and enhanced catalytic activity. *Energy Environ. Sci.* **2021**, *14*, 873–882. [CrossRef]
52. Yang, J.; Hu, S.; Shi, L.; Hoang, S.; Yang, W.; Fang, Y.; Liang, Z.; Pan, C.; Zhu, Y.; Li, L.; et al. Oxygen Vacancies and Lewis Acid Sites Synergistically Promoted Catalytic Methane Combustion over Perovskite Oxides. *Environ. Sci. Technol.* **2021**, *55*, 9243–9254. [CrossRef]
53. Li, X.; Li, M.; Ma, X.; Miao, J.; Ran, R.; Zhou, W.; Wang, S.; Shao, Z. Nonstoichiometric perovskite for enhanced catalytic oxidation through excess A-site cation. *Chem. Eng. Sci.* **2020**, *219*, 115596. [CrossRef]
54. Liang, P.; Meng, D.; Liang, Y.; Wang, Z.; Zhang, C.; Wang, S.; Zhang, Z. Cation deficiency tuned LaCoO3−δ perovskite for peroxymonosulfate activation towards bisphenol A degradation. *Chem. Eng. J.* **2020**, *409*, 128196. [CrossRef]
55. Islam, Q.A.; Majee, R.; Bhattacharyya, S. Bimetallic nanoparticle decorated perovskite oxide for state-of-the-art trifunctional electrocatalysis. *J. Mater. Chem. A* **2019**, *7*, 19453–19464. [CrossRef]
56. Ren, H.; Wang, Z.; Chen, X.; Jing, Z.; Qu, Z.; Huang, L. Effective mineralization of p-nitrophenol by catalytic ozonation using Ce-substituted $La_{1-x}Ce_xFeO_3$ catalyst. *Chemosphere* **2021**, *285*, 131473. [CrossRef]
57. Wang, Y.; Gong, Y.; Lin, N.; Yu, L.; Du, B.; Zhang, X. Enhanced removal of Cr(VI) from aqueous solution by stabilized nanoscale zero valent iron and copper bimetal intercalated montmorillonite. *J. Colloid Interface Sci.* **2022**, *606*, 941–952. [CrossRef]
58. Wu, M.; Li, H.; Ma, S.; Chen, S.; Xiang, W. Boosting the surface oxygen activity for high performance Iron-based perovskite oxide. *Sci. Total. Environ.* **2021**, *795*, 148904. [CrossRef]
59. Ding, J.; Liu, J.; Yang, Y.; Zhao, L.; Yu, Y. Understanding A-site tuning effect on formaldehyde catalytic oxidation over La-Mn perovskite catalysts. *J. Hazard. Mater.* **2022**, *422*, 126931. [CrossRef]

60. Zhao, D.; Yang, Y.; Gao, Z.; Tian, Y.; Zhang, J.; Jiang, Z.; Li, X. A-site defects in LaSrMnO3 perovskite-based catalyst promoting NO storage and reduction for lean-burn exhausts. *J. Rare Earths* **2021**, *39*, 959–968. [CrossRef]
61. Han, P.; Li, X.; Jin, C.; Tan, X.; Sun, W.; Wang, S.; Ding, F.; Li, X.; Jin, H.; Sun, C.; et al. Cation deviated stoichiometry Ca1.1ZrO3 perovskite as an efficient ozonation catalyst for m-cresol wastewater degradation. *Chem. Eng. J.* **2022**, *429*, 132218. [CrossRef]
62. You, M.; Gui, L.; Ma, X.; Wang, Z.; Xu, Y.; Zhang, J.; Sun, J.; He, B.; Zhao, L. Electronic tuning of SrIrO3 perovskite nanosheets by sulfur incorporation to induce highly efficient and long-lasting oxygen evolution in acidic media. *Appl. Catal. B* **2021**, *298*, 120562. [CrossRef]
63. Han, X.; Liu, P.; Ran, R.; Wang, W.; Zhou, W.; Shao, Z. Non-metal fluorine doping in Ruddlesden–Popper perovskite oxide enables high-efficiency photocatalytic water splitting for hydrogen production. *Mater. Today Energy* **2022**, *23*, 100896. [CrossRef]
64. Saloaro, M.; Liedke, M.; Angervo, I.; Butterling, M.; Hirschmann, E.; Wagner, A.; Huhtinen, H.; Paturi, P. Exploring the anti-site disorder and oxygen vacancies in Sr2FeMoO6 thin films. *J. Magn. Magn. Mater.* **2021**, *540*, 168454. [CrossRef]
65. Chen, X.; Zhang, T.; Yu, Y.; Cai, X.; Gao, T.; Zhang, T.; Sun, H.; Gu, C.; Gu, Z.; Zhu, Y.; et al. Rewritable High-Mobility Electrons in Oxide Heterostructure of Layered Perovskite/Perovskite. *ACS Appl. Mater. Interfaces* **2021**, *13*, 7812–7821. [CrossRef] [PubMed]
66. Yang, B.; Bian, J.; Wang, L.; Wang, J.; Du, Y.; Wang, Z.; Wu, C.; Yang, Y. Enhanced photocatalytic activity of perovskite $NaNbO_3$ by oxygen vacancy engineering. *Phys. Chem. Chem. Phys.* **2019**, *21*, 11697–11704. [CrossRef] [PubMed]
67. Liu, G.; Li, J.; Fu, J.; Jiang, G.; Lui, G.; Luo, D.; Deng, Y.; Zhang, J.; Cano, Z.P.; Yu, A.; et al. An Oxygen-Vacancy-Rich Semiconductor-Supported Bifunctional Catalyst for Efficient and Stable Zinc–Air Batteries. *Adv. Mater.* **2018**, *31*, 1806761. [CrossRef] [PubMed]
68. Liu, H. *Study on Defect Regulation and Photocatalytic and Electrocatalytic Properties in Transition Metal Compounds*; University of Science and Technology of China: Hefei, China, 2021; p. 000502.
69. Wang, Y.; Zhou, T.; Jiang, K.; Da, P.; Peng, Z.; Tang, J.; Kong, B.; Cai, W.-B.; Yang, Z.; Zheng, G. Reduced Mesoporous Co_3O_4Nanowires as Efficient Water Oxidation Electrocatalysts and Supercapacitor Electrodes. *Adv. Energy Mater.* **2014**, *4*, 1400696. [CrossRef]
70. Sun, W.; Wei, H.; An, L.Y.; Jin, C.; Wu, H.; Xiong, Z.-A.; Pu, C.; Sun, C. Oxygen vacancy mediated La1-xCexFeO3-δ perovskite oxides as efficient catalysts for CWAO of acrylic acid by A-site Ce doping. *Appl. Catal. B* **2019**, *245*, 20–28. [CrossRef]
71. Zhang, W.; Liu, Z.; Chen, P.; Zhou, G.; Liu, Z.; Xu, Y. Preparation of Supported Perovskite Catalyst to Purify Membrane Concentrate of Coal Chemical Wastewater in UV-Catalytic Wet Hydrogen Peroxide Oxidation System. *Int. J. Environ. Res. Public Heal.* **2021**, *18*, 4906. [CrossRef]
72. Neagu, D.; Oh, T.-S.; Miller, D.N.; Ménard, H.; Bukhari, S.M.; Gamble, S.R.; Gorte, R.J.; Vohs, J.M.; Irvine, J.T.S. Nano-socketed nickel particles with enhanced coking resistance grown in situ by redox exsolution. *Nat. Commun.* **2015**, *6*, 8120. [CrossRef]
73. Wang, X.; Li, X.; Chu, X.; Cao, R.; Qian, J.; Cong, Y.; Huang, K.; Wang, J.; Redshaw, C.; Sarangi, R.; et al. Manipulating Surface Termination of Perovskite Manganate for Oxygen Activation. *Adv. Funct. Mater.* **2021**, *31*, 2006439. [CrossRef]
74. Kim, K.; Koo, B.; Jo, Y.-R.; Lee, S.; Kim, J.K.; Kim, B.-J.; Jung, W.; Han, J.W. Control of transition metal–oxygen bond strength boosts the redox ex-solution in a perovskite oxide surface. *Energy Environ. Sci.* **2020**, *13*, 3404–3411. [CrossRef]
75. Oh, J.H.; Kwon, B.W.; Cho, J.; Lee, C.H.; Kim, M.K.; Choi, S.H.; Yoon, S.P.; Han, J.H.; Nam, S.W.; Kim, J.Y.; et al. Importance of Exsolution in Transition-Metal (Co, Rh, and Ir)-Doped $LaCrO_3$Perovskite Catalysts for Boosting Dry Reforming of CH_4Using $CO_2$for Hydrogen Production. *Ind. Eng. Chem. Res.* **2019**, *58*, 6385–6393. [CrossRef]
76. Li, Q.; Zhu, X.; Yang, J.; Yu, Q.; Zhu, X.; Chu, J.; Du, Y.; Wang, C.; Hua, Y.; Li, H.; et al. Plasma treated Bi_2WO_6 ultrathin nanosheets with oxygen vacancies for improved photocatalytic CO_2 reduction. *Inorg. Chem. Front.* **2020**, *7*, 597–602. [CrossRef]
77. Tong, B.; Meng, G.; Deng, Z.; Horprathum, M.; Klamchuen, A.; Fang, X. Surface oxygen vacancy defect engineering of p-$CuAlO_2$*via* Ar&H_2 plasma treatment for enhancing VOCs sensing performances. *Chem. Commun.* **2019**, *55*, 11691–11694. [CrossRef]
78. Selvadurai, A.P.B.; Xiong, T.; Huang, P.; Tan, Q.; Huang, Y.; Yang, H.; Balogun, M.-S.J.T. Tailoring the cationic and anionic sites of $LaFeO_3$-based perovskite generates multiple vacancies for efficient water oxidation. *J. Mater. Chem. A* **2021**, *9*, 16906–16916. [CrossRef]
79. Mishra, A.; Li, T.; Li, F.; Santiso, E.E. Oxygen Vacancy Creation Energy in Mn-Containing Perovskites: An Effective Indicator for Chemical Looping with Oxygen Uncoupling. *Chem. Mater.* **2018**, *31*, 689–698. [CrossRef]
80. Kang-Wen, Q.; Xi, C.; Zhang, Y.; Zhang, R.; Li, Z.; Sheng, G.-R.; Liu, H.; Dong, C.-K.; Chen, Y.-J.; Du, X.-W. Laser-induced oxygen vacancies in $FeCo_2O_4$ nanoparticles for boosting oxygen evolution and reduction. *Chem. Commun.* **2019**, *55*, 8579–8582. [CrossRef]
81. Haselmann, U.; Suyolcu, Y.E.; Wu, P.-C.; Ivanov, Y.P.; Knez, D.; van Aken, P.A.; Chu, Y.-H.; Zhang, Z. Negatively Charged In-Plane and Out-Of-Plane Domain Walls with Oxygen-Vacancy Agglomerations in a Ca-Doped Bismuth-Ferrite Thin Film. *ACS Appl. Electron. Mater.* **2021**, *3*, 4498–4508. [CrossRef] [PubMed]
82. Badreldin, A.; Abusrafa, A.E.; Abdel-Wahab, A. Oxygen-deficient perovskites for oxygen evolution reaction in alkaline media: A review. *Emergent Mater.* **2020**, *3*, 567–590. [CrossRef]
83. Li, X.; Sun, Y.; Ren, F.; Bai, Y.; Cheng, Z. Smart oxygen vacancy engineering to enhance water oxidation efficiency by separating the different effects of bulk and surface vacancies. *Mater. Today Energy* **2021**, *19*, 100619. [CrossRef]
84. Ma, X.; Xiao, M.; Yang, X.; Yu, X.; Ge, M. Boosting benzene combustion by engineering oxygen vacancy-mediated Ag/CeO2-Co3O4 catalyst via interfacial electron transfer. *J. Colloid Interface Sci.* **2021**, *594*, 882–890. [CrossRef]

85. Zhu, Y.; Li, W.; Liu, Y.; Zhu, X.; Yang, W. Selection of oxygen permeation models for different mixed ionic-electronic conducting membranes. *AIChE J.* **2017**, *63*, 4043–4053. [CrossRef]
86. Wang, J.; Yang, T.; Lei, L.; Huang, K. Ta-Doped $SrCoO_{3-\delta}$ as a promising bifunctional oxygen electrode for reversible solid oxide fuel cells: A focused study on stability. *J. Mater. Chem. A* **2017**, *5*, 8989–9002. [CrossRef]
87. Asnavandi, M.; Yin, Y.; Li, Y.; Sun, C.; Zhao, C. Promoting Oxygen Evolution Reactions through Introduction of Oxygen Vacancies to Benchmark NiFe–OOH Catalysts. *ACS Energy Lett.* **2018**, *3*, 1515–1520. [CrossRef]
88. Wu, M.; Luo, M.; Guo, M.; Jia, L. Sugarcane Bagasse Hydrolysis by Metal Ions Mediated Synthesis of Perovskite $LaCoO_3$ and the Photocatalytic Performance for Hydrogen from Formaldehyde Solution under Visible Light. *ACS Sustain. Chem. Eng.* **2017**, *5*, 11558–11565. [CrossRef]
89. Shi, X.; Zheng, H.; Kannan, A.M.; Pérez-Salcedo, K.; Escobar, B. Effect of Thermally Induced Oxygen Vacancy of α-MnO_2 Nanorods toward Oxygen Reduction Reaction. *Inorg. Chem.* **2019**, *58*, 5335–5344. [CrossRef]
90. Ma, M.; Peng, L.; Li, J.; Zhang, Y.; Wang, Z.; Bi, J.; Gao, D.; Wu, J. Oxygen vacancy engineering and superior sensing properties of hematite prepared via a one-step treatment. *Sensors Actuators B* **2021**, *339*, 129907. [CrossRef]
91. Liang, J.; Xu, Q.; Teng, X.; Guan, W.; Lu, C. Superoxide-Triggered Luminol Electrochemiluminescence for Detection of Oxygen Vacancy in Oxides. *Anal. Chem.* **2020**, *92*, 1628–1634. [CrossRef]
92. Magray, M.A.; Ikram, M.; Najim, M. Impact of oxygen vacancies to control the magnetic and electronic properties of the La2CoMnO6 system. *J. Magn. Magn. Mater.* **2021**, *529*, 167857. [CrossRef]
93. Tran, S.B.T.; Choi, H.; Oh, S.; Park, J.Y. Defective Nb2O5-supported Pt catalysts for CO oxidation: Promoting catalytic activity via oxygen vacancy engineering. *J. Catal.* **2019**, *375*, 124–134. [CrossRef]
94. Zhang, B.; Zhang, S.; Liu, B. Effect of oxygen vacancies on ceria catalyst for selective catalytic reduction of NO with NH3. *Appl. Surf. Sci.* **2020**, *529*, 147068. [CrossRef]
95. Zhai, Z.; Yan, W.; Dong, L.; Deng, S.; Wilkinson, D.P.; Wang, X.; Zhang, L.; Zhang, J. Catalytically active sites of MOF-derived electrocatalysts: Synthesis, characterization, theoretical calculations, and functional mechanisms. *J. Mater. Chem. A* **2021**, *9*, 20320–20344. [CrossRef]
96. Wang, H.B.; Liang, W.; Luo, Z.L.; Liu, Q.Q.; Huang, H.L.; Yang, M.M.; Yang, Y.J.; Hu, S.X.; Jiang, Z.; Li, S.; et al. Location of oxygen vacancies in Sr2CuO3+δ single crystal determined by polarized EXAFS at Cu K-edge. *Solid State Commun.* **2019**, *299*, 113649. [CrossRef]
97. Xie, J.; Bai, P.; Wang, C.; Chen, N.; Chen, W.; Duan, M.; Wang, H. Enhancing H_2 Evolution by Adjusting Oxygen Species at Perovskite $SrTiO_3$. *ACS Appl. Energy Mater.* **2022**, *5*, 9559–9570. [CrossRef]
98. Jing, J.; Pervez, N.; Sun, P.; Cao, C.; Li, B.; Naddeo, V.; Jin, W.; Zhao, Y. Highly efficient removal of bisphenol A by a novel Co-doped LaFeO3 perovskite/PMS system in salinity water. *Sci. Total. Environ.* **2021**, *801*, 149490. [CrossRef]
99. Li, J.; Xu, M.; Yao, G.; Lai, B. Enhancement of the degradation of atrazine through CoFe2O4 activated peroxymonosulfate (PMS) process: Kinetic, degradation intermediates, and toxicity evaluation. *Chem. Eng. J.* **2018**, *348*, 1012–1024. [CrossRef]
100. Chen, L.; Liu, Y.; Fang, X.; Cheng, Y. Simple strategy for the construction of oxygen vacancies on alpha-MnO2 catalyst to improve toluene catalytic oxidation. *J. Hazard. Mater.* **2021**, *409*, 125020. [CrossRef]
101. Zeng, J.; Xie, H.; Liu, Z.; Liu, X.; Zhou, G.; Jiang, Y. Oxygen vacancy induced MnO_2 catalysts for efficient toluene catalytic oxidation. *Catal. Sci. Technol.* **2021**, *11*, 6708–6723. [CrossRef]
102. Yang, Q.; Du, J.; Li, J.; Wu, Y.; Zhou, Y.; Yang, Y.; Yang, D.; He, H. Thermodynamic and Kinetic Influence of Oxygen Vacancies on the Solar Water Oxidation Reaction of alpha-Fe_2O_3 Photoanodes. *ACS Appl. Mater. Interfaces* **2020**, *12*, 11625–11634. [CrossRef] [PubMed]
103. Chen, D.; Niu, F.; Qin, L.; Wang, S.; Zhang, N.; Huang, Y. Defective BiFeO3 with surface oxygen vacancies: Facile synthesis and mechanism insight into photocatalytic performance. *Sol. Energy Mater. Sol. Cells* **2017**, *171*, 24–32. [CrossRef]
104. Kwon, O.; Kim, Y.I.; Kim, K.; Kim, J.C.; Lee, J.H.; Park, S.S.; Han, J.W.; Kim, Y.M.; Kim, G.; Jeong, H.Y. Probing One-Dimensional Oxygen Vacancy Channels Driven by Cation–Anion Double Ordering in Perovskites. *Nano Lett.* **2020**, *20*, 8353–8359. [CrossRef] [PubMed]
105. Yang, X.; Yu, X.; Jing, M.; Song, W.; Liu, J.; Ge, M. Defective $Mn_xZr_{1-x}O_2$ Solid Solution for the Catalytic Oxidation of Toluene: Insights into the Oxygen Vacancy Contribution. *ACS Appl. Mater. Interfaces* **2019**, *11*, 730–739. [CrossRef] [PubMed]
106. Guo, S.; Liu, G.; Zhang, Y.; Liu, Y. Oxygen vacancies boosted Co-Co2C catalysts for higher alcohols synthesis from syngas. *Appl. Surf. Sci.* **2022**, *576*, 151846. [CrossRef]
107. Rao, Y.; Zhang, Y.; Han, F.; Guo, H.; Huang, Y.; Li, R.; Qi, F.; Ma, J. Heterogeneous activation of peroxymonosulfate by LaFeO3 for diclofenac degradation: DFT-assisted mechanistic study and degradation pathways. *Chem. Eng. J.* **2018**, *352*, 601–611. [CrossRef]
108. Yang, Y.; Li, X.; Jie, B.; Zheng, Z.; Li, J.; Zhu, C.; Wang, S.; Xu, J.; Zhang, X. Electron structure modulation and bicarbonate surrounding enhance Fenton-like reactions performance of Co-Co PBA. *J. Hazard. Mater.* **2022**, *437*, 129372. [CrossRef]
109. Liu, N.; Dai, W.; Fei, F.; Xu, H.; Lei, J.; Quan, G.; Zheng, Y.; Zhang, X.; Tang, L. Insights into the photocatalytic activation persulfate by visible light over ReS2/MIL-88B(Fe) for highly efficient degradation of ibuprofen: Combination of experimental and theoretical study. *Sep. Purif. Technol.* **2022**, *297*, 121545. [CrossRef]
110. Liu, N.; Fei, F.; Dai, W.; Lei, J.; Bi, F.; Wang, B.; Quan, G.; Zhang, X.; Tang, L. Visible-light-assisted persulfate activation by SnS2/MIL-88B(Fe) Z-scheme heterojunction for enhanced degradation of ibuprofen. *J. Colloid Interface Sci.* **2022**, *625*, 965–977. [CrossRef]

111. Yang, L.; Jiao, Y.; Xu, X.; Pan, Y.; Su, C.; Duan, X.; Sun, H.; Liu, S.; Wang, S.; Shao, Z. Superstructures with Atomic-Level Arranged Perovskite and Oxide Layers for Advanced Oxidation with an Enhanced Non-Free Radical Pathway. *ACS Sustain. Chem. Eng.* **2022**, *10*, 1899–1909. [CrossRef]
112. Nie, Z.; Ma, L.; Xi, X.; Liu, Y.; Zhao, L. First-principles Study on Nanoscale Tungsten Oxide: A Review. *J. Inorg. Mater.* **2021**, *36*, 1125. [CrossRef]
113. Hoffmann, M.; Antonov, V.N.; Bekenov, L.V.; Kokko, K.; Hergert, W.J.; Ernst, A. Variation of magnetic properties of Sr_2FeMoO_6 due to oxygen vacancies. *J. Phys. Condens. Matter* **2018**, *30*, 305801. [CrossRef] [PubMed]
114. Wang, Y.; Zhang, Z.; Cheng, J.; Zhang, Q.; Tang, W.; Yang, K. Creating a two-dimensional hole gas in a polar/polar $LaAlO_3/KTaO_3$ perovskite heterostructure. *J. Mater. Chem. C* **2020**, *8*, 14230–14237. [CrossRef]